Enhanced sequential osteosarcoma therapy using a 3D-Printed bioceramic scaffold combined with 2D nanosheets via NIR-II photothermal-chemodynamic synergy

Guangyu Jian [a,1], Si Wang [a,1], Xinlu Wang [a], Qinyi Lu [a], Xingyu Zhu [a], Shucheng Wan [a], Shan Wang [a], Dize Li [a], Chao Wang [b], Qingqing He [a,***], Tao Chen [a,**], Jinlin Song [a,*]

[a] The Affiliated Stomatological Hospital of Chongqing Medical University, Chongqing Key Laboratory of Oral Diseases, Chongqing Municipal Key aboratory of Oral Biomedical Engineering of Higher Education, Chongqing Municipal Health Commission Key Laboratory of Oral Biomedical Engineering, Chongqing, 401147, PR China
[b] Key Laboratory of Biomechanics and Mechanobiology, Ministry of Education, Beijing Advanced Innovation Center for Biomedical Engineering, School of Biological Science and Medical Engineering, School of Engineering Medicine, Beihang University, Beijing 100083, PR China

A R T I C L E   I N F O

A B S T R A C T

Background: Osteosarcoma (OS) is a malignant tumor originating from primitive mesenchymal cells, characterized by rapid metastasis, high invasiveness, and significant mortality. The primary challenges in OS management include the effective elimination of residual tumor cells to prevent recurrence and the repair of extensive bone defects caused by surgical intervention.
Objective: This study aims to develop an innovative biomimetic 3D-printed bioactive glass ceramic (BGC) scaffold modified with two-dimensional nanosheets to address both tumor ablation and bone tissue repair.
Materials and methods: The nanosheets were constructed via ellagic acid (EA) and ruthenium (Ru) coordination, leveraging the non-topological adhesion properties of catechol in EA to deposit the nanosheets onto the BGC scaffold (EARu-BGC). The therapeutic effects of EARu-BGC were evaluated *in vitro* and *in vivo*.
Results: EARu-BGC sequentially responds to the local microenvironment during OS treatment. During the tumor ablation phase, EARu-BGC induced ferroptosis through the synergistic effects of photothermal and chemodynamic therapy, achieving over 90 % tumor cell ablation and significantly inhibiting tumor volume and weight. In the bone tissue repair phase, EARu-BGC exhibited adaptive ROS scavenging and facilitated a pro-healing microenvironment, promoting osteogenic differentiation. The gradual degradation of the BGC scaffold provided essential minerals and space for new bone formation. In vivo experiments demonstrated that EARu-BGC significantly enhanced osteogenesis, increasing the trabecular number to 1.51 ± 0.15/mm and reducing trabecular separation to 1.50 ± 0.04 mm.
Conclusion: The EARu-BGC scaffold presents a promising multifunctional platform for OS treatment by effectively balancing antitumor efficacy with bone repair capabilities.

1. Introduction

Osteosarcoma (OS) is a highly aggressive malignant tumor originating from primitive transformed mesenchymal cells and is characterized by the production of neoplastic osteoids [1,2]. OS is known for its pronounced invasiveness, rapid metastasis, and high mortality rates [3, 4]. Currently, the standard clinical treatment for OS involves surgical resection combined with chemotherapy [5,6]. However, the aggressive nature of OS combined with the complex anatomy of bone structures typically precludes complete radical resection, leading to a considerable risk of local recurrence. Furthermore, extensive bone defects caused by surgery frequently exceed the intrinsic capacity of bone tissue for repair

and regeneration [7–9]. This scenario not only exposes patients to prolonged pain and physical discomfort but also imposes severe psychological stress in addition to the societal burden. Consequently, multifunctional tissue-engineered biomaterials capable of eliminating bone tumors and promoting bone tissue regeneration are urgently needed.

Recent research has revealed that ferroptosis is a novel form of regulated cell death that has emerged as a promising avenue for cancer therapy [10]. Ferroptosis is driven by the iron-dependent accumulation of reactive oxygen species (ROS) and lipid peroxides along with the inactivation of key antioxidant systems such as glutathione peroxidase 4 (GPX4) [11,12]. Unlike apoptosis, which typically exhibits dysregulation in cancer cells, ferroptosis appears inducible across a broad spectrum of cancer types, including those resistant to conventional therapies [13,14]. Moreover, ferroptosis operates through unique signaling pathways and cellular mechanisms, offering the prospect of overcoming treatment resistance while selectively targeting malignant cells and sparing normal tissues [15,16]. Given these characteristics, the induction of ferroptosis is a potentially effective therapeutic strategy for OS.

Previous studies have demonstrated that therapies such as chemodynamic therapy (CDT), radiotherapy, photothermal therapy (PTT), and photodynamic therapy (PDT) can enhance the therapeutic efficacy against tumor [17]. Among these, CDT has gained considerable attention for its ability to induce ferroptosis by converting endogenous hydrogen peroxide (H_2O_2) in the tumor microenvironment into highly reactive hydroxyl radicals ($\cdot OH$) through Fenton or Fenton-like reactions [18]. The ROS generated by CDT subsequently damages cell membranes, cellular lipids, proteins, and DNA, leading to ferroptosis [19]. CDT offers the advantages of being minimally invasive and highly specific to tumor cells while minimizing off-target effects in normal tissues owing to the relatively low levels of H_2O_2 in non-tumorous environments [20,21]. However, the therapeutic efficacy of CDT is typically limited by elevated levels of intracellular glutathione (GSH), which neutralizes ROS and maintains redox homeostasis [22]. Consequently, the combination of CDT with other therapies is necessary to overcome the limitations of single-treatment approaches. PTT is a promising tumor ablation strategy that employs photothermal agents to generate localized hyperthermia under near-infrared (NIR) laser irradiation [23]. By elevating the localized temperature, PTT accelerates Fenton-like reactions, enhancing $\cdot OH$ production, amplifying oxidative stress, and then disrupting redox homeostasis [24]. Although PTT alone may lead to cellular thermotolerance via heat shock proteins (HSPs) overexpression, ROS-induced oxidative damage can inhibit the expression and function of HSPs, thereby enhancing the efficacy of PTT [25]. Thus, the combination of PTT and CDT can amplify each other's effects, synergistically enhancing ferroptosis and achieving multiple effects on OS.

Following bone tumor ablation, effective bone tissue remodeling remains a significant challenge, particularly in addressing the structural and compositional complexity of the bone. Recent advancements in three-dimensional (3D)-printed bioactive glass ceramic (BGC) scaffolds present a promising solution because of their ability to mimic the intricate architecture and chemical profile of the bone tissue [26,27]. Studies have shown that the interconnected macroporous structure of 3D-printed BGC scaffolds, along with key constituent elements such as calcium (Ca), silicon (Si), and phosphorus (P), supports the attachment and proliferation of bone marrow mesenchymal stem cells (BMSCs), stimulates osteogenic differentiation, enhances angiogenesis *in vitro* [28], and initiates bone regeneration *in vivo* [29–31]. In addition, combined with advanced 3D printing technology, 3D-printed BGC scaffolds can be shaped longitudinally to meet the customization requirements for irregularly shaped bone defects [20,32,33]. Therefore, the combination of 3D-printed BGC scaffolds with PTT and CDT not only allows for precise tumor treatment but also facilitates the simultaneous repair of bone defects at the tumor site. This integrated approach provides a novel, multifunctional treatment strategy for OS.

In this study, we developed a multifunctional 3D-printed BGC scaffold with sequential capabilities for bone tumor ablation and bone tissue remodeling. This scaffold enhanced tumor ablation by inducing ferroptosis through the synergistic effects of PTT and CDT, while also facilitating subsequent bone tissue repair through microenvironmental adaptation and the osteogenic properties of the BGC scaffold (Fig. 1). Specifically, two-dimensional (2D) metal-polyphenol network (MPN) nanosheets, formed by coordinating ellagic acid (EA) with the transition metal ruthenium (Ru), were deposited onto 3D-printed BGC scaffolds. The scaffold enabled a tumor microenvironment-responsive mechanism, where PTT and CDT synergistically amplified ROS production and GSH depletion, effectively inducing ferroptosis to ablate the tumor. In addition, in a neutral microenvironment, the scaffold exhibited adaptive ROS-scavenging capabilities and supported the osteogenic differentiation of BMSCs, thereby aiding bone tissue regeneration. Additionally, EA, a biodegradable component within the nanosheet coating, accelerated new bone formation, whereas gradual degradation of the BGC scaffold provided essential minerals and structural support for the regenerated bone tissue. This multifunctional 3D-printed scaffold represents an innovative therapeutic approach for OS, offering both effective tumor eradication and enhanced bone regeneration.

2. Materials and Methods

2.1. Synthesis of EARu

EA (Purchased from Aladdin, China) was weighed and dissolved in distilled water to obtain a concentration of 24 mM, followed by vigorous shaking for 30 s. Then, 24 mL of $RuCl_3 \bullet 3H_2O$ (24 mM, Purchased from Aladdin, China) was added to 25 mL of the EA solution. After mixing, sodium hydroxide (1 M, Purchased from Aladdin, China) was slowly added to adjust the pH to 8.0. The mixture was vortexed vigorously at room temperature to ensure thorough mixing. Finally, the products were collected by centrifugation at 5000 revolutions per minute (rpm) for 15 min, washed thrice with ultrapure water, and placed in a freeze dryer overnight to obtain pure EARu.

2.2. Synthesis of BGC scaffolds

The BGC scaffolds were fabricated using a Digital Light Processing (DLP)-based additive manufacturing system under a UV light source at λ = 405 nm. The photosensitive ceramic resin composite material (slurry) consisted of a mixture of apatite/wollastonite (A-W) bioactive glass ceramic, purchased from Naton Medical Group (Beijing, China), and a proprietary resin formula. The nominal and real chemical composition of the A-W bioactive glass ceramic is shown in Table S1. Each sliced layer in the DLP process was set to a thickness of 30 μm, with an exposure time of 5 s. After completing the printing process, the scaffolds were detached from the support plate and thoroughly rinsed with sufficient distilled water to remove the residual liquid slurry. Subsequently, the samples were then heated to 600 °C at a rate of 2 °C/min and maintained at this temperature for 120 min. Following this, they were further heated to 1100 °C at a heating rate of 1 °C/min and held at this higher temperature for an additional 120 min. Subsequently, sintered BGC scaffolds were obtained.

2.3. Synthesis of EARu-BGC scaffolds

During the synthesis process of EARu, BGC scaffolds were immersed into the reaction solution for the deposition of nanosheets, followed by drying at 60 °C for 30 min. This procedure was repeated 1, 5, and 10 times to obtain the final EARu-BGC scaffolds, which were designated 1 EARu-BGC, 5 EARu-BGC, and 10 EARu-BGC, respectively.

2.4. Characterization of EARu and EARu-BGC scaffolds

To confirm the size and morphology of EARu, transmission electron
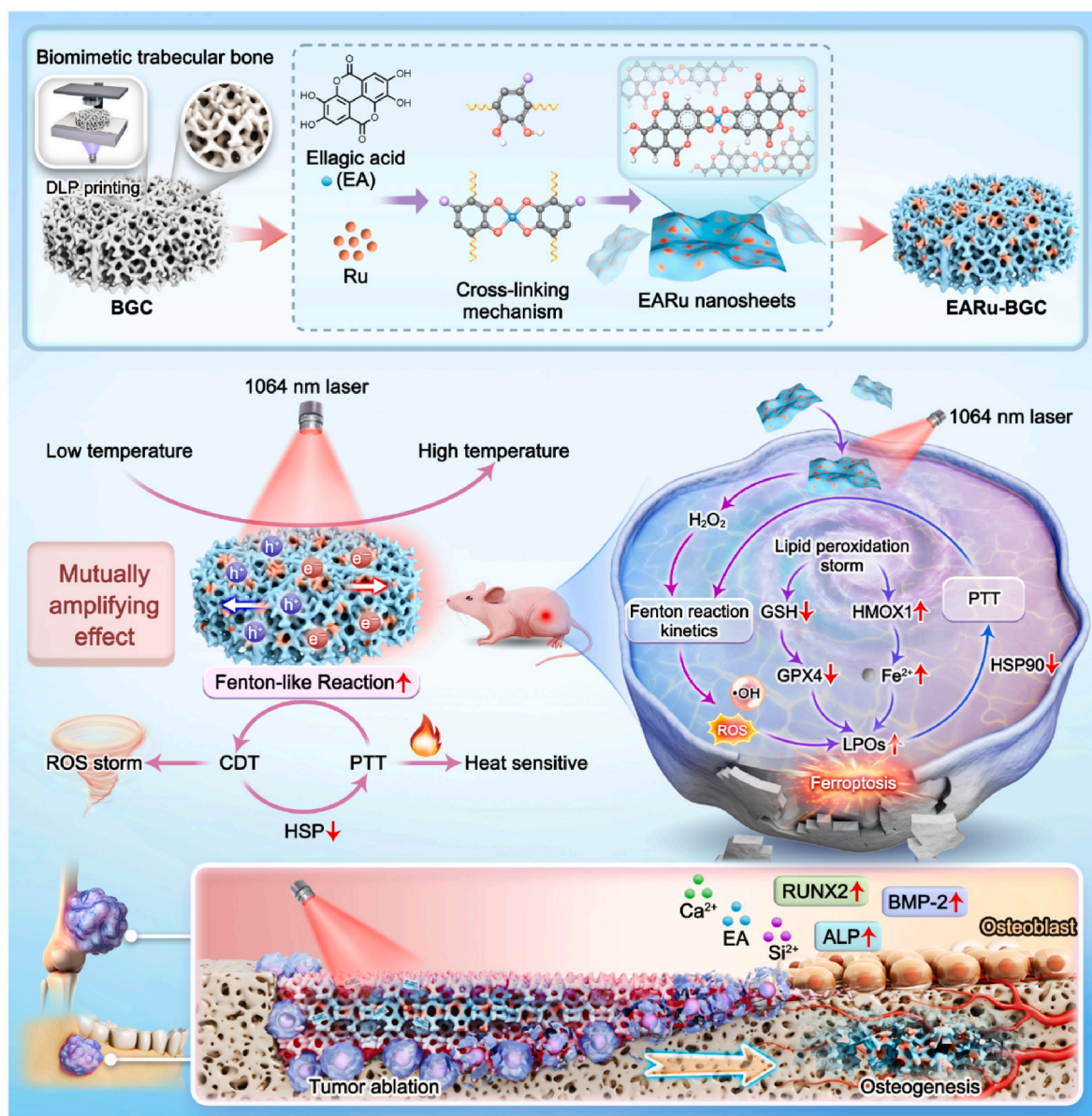
Fig. 1. Schematic illustrating the construction of the EARu-BGC scaffold and its sequential bone tumor ablation and bone tissue remodeling capabilities. First, EARu-BGC promotes ferroptosis through the synergistic enhancement of PTT and CDT to ablate OS, and then, it releases bioactive ions to achieve osteogenesis after OS ablation.

microscopy (TEM) images were obtained using a JEOL JEM 2100F (JEOL Ltd., Tokyo, Japan). Scanning electron microscopy (SEM) images, energy-dispersive X-ray spectroscopy (EDS), and elemental mapping were obtained using a ZEISS Sigma 300 (Carl Zeiss AG, Oberkochen, Germany). Atomic force microscopy (AFM) images were captured using a Bruker Dimension Icon (Bruker Corporation, Billerica, MA, USA). To verify the successful synthesis of EARu, Fourier transform infrared (FTIR) spectra were collected using a Nicolet IS 50 spectrometer (Thermo Fisher Scientific, Waltham, MA, USA). X-ray diffraction (XRD) patterns were characterized using an X'Pert PRO MPD (PANalytical, Almelo, Netherlands), and X-ray photoelectron spectroscopy (XPS) analysis was conducted using a K-Alpha spectrometer (Thermo Fisher Scientific, Waltham, MA, USA).After micro-CT scanning, the porosity and average pore size of BGC, 1EARu-BGC, 5EARu-BGC, and 10EARu-BGC were analyzed using Materialise Mimics software (Materialise NV, Leuven, Belgium).

2.5. TGA analysis of EA, EA + Ru, EARu and BGC, 1EARu-BGC, 5EARu-BGC, 10EARu-BGC

Thermogravimetric analysis (TGA) was performed using a Netzsch STA 449F3 thermal analyzer (Netzsch-Gerätebau GmbH, Selb, Germany) to assess the thermal stability and decomposition behavior of the samples. Approximately 100 mg of each sample (EA, EA + Ru (Ru 50 %), and EARu) was placed in an alumina crucible and heated from 30 °C to 1000 °C at a heating rate of 20 °C/min under a controlled atmosphere. The weight loss of the samples was continuously recorded as a function of temperature. The obtained TGA curves were analyzed to determine the thermal degradation profile, decomposition stages, and residual mass at elevated temperatures. The TGA analysis method for BGC, 1 EARu-BGC, 5 EARu-BGC, and 10 EARu-BGC was conducted following the same procedure as described above.

2.6. Ions release profile of EARu-BGC scaffolds

EARu-BGC scaffolds were immersed in buffer solutions at pH 5.5 and pH 7.0 and incubated at 37 °C with continuous shaking at 100 rpm to evaluate ion release. At predetermined time points, supernatants were collected and analyzed for Ru concentrations using Inductively Coupled Plasma Mass Spectrometry (ICP-MS) and for Ca and Si ion concentrations using Inductively Coupled Plasma Optical Emission Spectroscopy (ICP-OES). Ru ion concentrations were determined using an Agilent 7850 ICP-MS (Agilent Technologies, Santa Clara, CA, USA), while Ca and Si ion concentrations were measured using an Agilent 5110 ICP-OES (Agilent Technologies, Santa Clara, CA, USA). The collected supernatants were filtered through a 0.22 μm membrane and diluted with deionized water to ensure compliance with the calibration range. Standard solutions were prepared for calibration, and internal standards were used to enhance measurement accuracy. The results were analyzed based on the calibration curve and reported in ppm.

2.7. In vitro photothermal performance of EARu-BGC scaffolds

The different scaffolds were individually subjected to 1064 nm laser irradiation at a power density of 0.5 W/cm^2, and the surface temperature of the scaffolds was monitored using an infrared thermal imager. Five "off-on" laser cycles were performed to evaluate the photothermal stabilities of the scaffolds. Subsequently, the photothermal performance of EARu-BGC was assessed at various power densities (0.25, 0.5, 0.75, and 1.0 W/cm^2) to identify the optimal laser power density for tumor ablation. Finally, the photothermal conversion efficiency of EARu was calculated.

2.8. $^1O_2$ and ·OH generation

The peroxidase (POD)-like activity of EARu was assessed using a 3,3′,5,5′-tetramethylbenzidine (TMB) assay in a sodium acetate/acetic acid (NaAC/HAC) buffer solution (pH 4.5). The reaction system contained H_2O_2, and EARu was added at concentrations of 0, 100, 200, 500, and 1000 μg/mL in the presence of 10 mM H_2O_2. Additionally, H_2O_2 was introduced into a 200 μg/mL EARu solution at concentrations of 0, 1, 2, 5, 10, and 20 mM. Subsequently, 100 μL of TMB (10 mmol/L) was added, and the system was allowed to react for 10 min. Color changes in the solution were recorded using a camera, and the absorbance spectra of the reacted solutions were measured at 370 nm using a PerkinElmer EnSpire multifunctional microplate luminescence detector (PerkinElmer, Waltham, MA, USA). For $^1O_2$ detection, a NaAC/HAC buffer solution (pH 4.5) containing 20 μg/mL of 1,3-diphenylisobenzofuran (DPBF), 10 mM H_2O_2, and varying concentrations of EARu (0, 50, 100, 200, 500, and 1000 μg/mL) was prepared in a total volume of 2 mL. The reaction was allowed to proceed for 0, 2, 5, 10, and 20 min, and the absorbance spectra of the reacted solutions were measured at 410 nm to assess the changes over time. TMB and DPBF was purchased from Sigma-Aldrich (St. Louis, MO, USA), and NaAC/HAC buffer was obtained from Macklin (Shanghai, China).

2.9. Evaluation of scavenging ability of ·OH and RNS

The scavenging abilities of these compounds were also evaluated. ·OH and RNS, 50 μL of EARu solutions at various concentrations were mixed with 13 μL of 5 mmol/L H_2O_2 solution (prepared from 30 % H_2O_2), 13 μL FeSO$_4$ (1 mM) and 13 μL of 0.1 mg/mL TMB solution (prepared in DMSO) in 900 μL of phosphate-buffered saline (PBS) buffer (pH 7.4). The final concentration of EARu was determined as previously described. After incubation at room temperature (25 °C) for 15 min, the absorbance at 370 nm was measured using a multifunctional microplate luminescence detector.

For the DPPH assay, DPPH was dissolved in anhydrous ethanol, and EARu solutions at the same concentrations (0, 100, 200, 500 and 1000

μg/mL) were prepared in anhydrous ethanol. DPPH was added to a final concentration of 0.1 mmol/L. The reaction mixture was incubated at room temperature in the dark for 15 min, following which absorbance was measured at 517 nm using a multifunctional microplate luminescence detector. FeSO$_4$ and DPPH was purchased from Sigma-Aldrich (St. Louis, MO, USA).

2.10. Electron spin resonance (ESR) measurement

Following the protocol outlined in Method 4.6, 900 μL of NaAC/HAC buffer solution was added to a reaction vessel, followed by the addition of 100 μL of EARu to achieve a final concentration of 500 μg/mL. Subsequently, 20 μL of H_2O_2 was introduced, resulting in a final concentration of 10 mM. The reaction was allowed to proceed for approximately 15 min at ambient temperature under NIR irradiation. To capture ·OH, 5,5-dimethyl-1-pyrroline-N-oxide (DMPO, 0.1 M) was employed, while 2,2,6,6-tetramethylpiperidine (TEMP, 50 mM) was used to capture $^1O_2$. Electron spin resonance (ESR) spectra were recorded using a Bruker EMXplus ESR spectrometer (Bruker, Karlsruhe, Germany) to confirm the generation of reactive oxygen specie.

2.11. GSH depletion

GSH consumption was quantified using 5,5′-dithiobis-(2-nitrobenzoic acid) (DTNB, Sigma-Aldrich, USA). The experiment was organized into four groups: 1) GSH, 2) GSH + DTNB + H_2O_2, 3) GSH + DTNB + EARu, and 4) GSH + DTNB + EARu + H_2O_2. A total of 2 mL of the reaction mixture, which included GSH (10 mM), DTNB (100 μg/mL), EARu (500 μg/mL), and H_2O_2 (10 mM), was prepared. After allowing the reaction to proceed for 1 min, the absorbance spectra of the reacted solutions were measured at 412 nm to assess the changes.

2.12. In vitro cell culture study

143B (ATCC, Manassas, USA) and rBMSC were incubated in Dulbecco's Modified Eagle's medium (DMEM, Corning, USA) supplemented with 10 % fetal bovine serum (FBS, Gibco, USA), 1 % penicillin-streptomycin (HyClone, USA) in a humidified incubator (37 °C, 5 % CO_2). To examine rBMSC osteo-differentiation, we supplemented the growth medium with β-glycerophosphate (10 mM), L-ascorbic acid (50 g/mL), and dexamethasone (10 nM) (osteogenic medium, OM).

2.13. In vitro cytotoxicity and tumor cell ablation assays

rBMSCs (1 × 10^4 per well) were seeded in a 48-well plate and incubated for 24 h. The culture medium was then replaced with fresh medium containing varying concentrations of EARu (0, 50, 100, 200, and 500 μg/mL). After an additional 24-h incubation, the cells were gently washed twice with PBS, and 200 μL of CCK-8 medium diluent was added to each well. Following a further 1-h incubation, optical density was measured at 450 nm using a microplate reader.

For the tumor cell ablation experiment, 143B cells (1 × 10^4 per well) were seeded in a 48-well plate and divided into seven groups: 1) Ctrl group, 2) H_2O_2 group, 3) NIR II group, 4) EARu group, 5) EARu + NIR II group, 6) EARu + H_2O_2 group, and 7) EARu + H_2O_2 + NIR II group. The NIR II laser was operated at 1064 nm with an irradiation time of 5 min at a power density of 1.0 W/cm^2. The concentration of H_2O_2 was 100 μM. After 24 h of incubation, cell viability was assessed using a previously described method.

2.14. Live/dead cell staining and intracellular ROS detection

In accordance with Method 4.10: Tumor Cell Ablation Experiment, 4 h post-stimulation, the cells were washed twice with PBS and subsequently stained with calcein-AM/PI working solution for 30 min. After staining, the cells were washed twice with PBS, and fluorescence images

were acquired using confocal laser scanning microscopy (CLSM, Leica Microsystems, Wetzlar, Germany). For flow cytometric analysis, the procedure was the same, except that 143 B cells were seeded in a 24-well plate. To determine endogenous ROS, after 4 h, the cells were washed twice with PBS and stained with DCFH-DA (Beyotime, Shanghai, China) working solution for 30 min. Finally, the cells were washed twice with PBS and fluorescence images were obtained using CLSM.

2.15. Intracellular GSH level assessment

Adherent 143B cells (2.5×10^4 per well) were incubated with the following treatments in the 24-well plate for 24 h: 1) Ctrl group, 2) H_2O_2 group, 3) NIR II group, 4) EARu group, 5) EARu + NIR II group, 6) EARu + H_2O_2 group, and 7) EARu + H_2O_2 + NIR II group. Subsequently, the amount of GSH was evaluated using a GSH assay kit, according to the manufacturer's instructions.

2.16. Transcriptome sequencing

The 143B cells (5.0×10^4 per well) were incubated with 500 μg/mL EARu and 200 μM H_2O_2 under NIR II laser irradiation for 5 min (1.0 W/cm^2). RNA samples were thermally denatured, and mRNA was enriched using oligo(dT) beads. The mRNA was fragmented, followed by the synthesis of first- and second-strand cDNA. cDNA ends were repaired, adenine bases were added, and adapters were ligated. Subsequently, PCR amplification was performed. The quality of the sequencing library was checked, and the PCR products were denatured and circularized using linear DNA digestion. Finally, rolling circle replication generated DNA nanoballs (DNBs) for sequencing using combinatorial probe-anchor synthesis (cPAS) technology on a high-density nanochip, and the raw data obtained from sequencing were filtered using Fastp (v0.23.4), which removed reads containing adapters and low-quality reads. The clean data were aligned to the reference genome (http://asia.ensembl.org/Homo_sapiens/Info/Index) using the Tophat2 software (v2.1.1). Subsequently, read quantification of gene expression was performed using HTSeq (v2.0.5). Differential gene expression analysis was conducted using DESeq2 (v1.4.5), with the criteria of P value < 0.05 and log2FoldChange > |1|. Kyoto Encyclopedia of Genes and Genomes (KEGG), Gene Ontology (GO) enrichment analyses, and Gene Set Enrichment Analysis (GSEA) were performed using ClusterProfiler (v4.12.6) and annotated with org.hs.eg.db (v3.19.1). GSVA analysis was conducted using R software GSVA (v 2.0.0), annotated with Reactome gene sets from the MSigDB database (www.gsea-msigdb.org/gsea/msigdb).

2.17. Ferroptosis-related protein expression evaluated by Western blot

Adhered 143B cells (2.5×10^4 per well) were incubated in a 24-well plate for 24 h. Following incubation, the cells were lysed using RIPA lysis buffer, and the total protein content was determined using a BCA Protein Assay Kit (Beyotime, Shanghai, China), followed by analysis using 12 % sodium dodecyl sulfate-polyacrylamide gel electrophoresis (SDS-PAGE, Epizyme, Shanghai, China). Subsequently, the proteins were incubated with primary antibodies of interest. After incubation with the primary antibody, the proteins were washed to remove unbound antibodies. Subsequently, the cells were incubated with an appropriate secondary antibody conjugated to the detection enzyme or fluorophore. The resulting signals were visualized using enhanced chemiluminescence.

2.18. In vivo tumor ablation therapy

All animal experiments were approved by the Animal Experiment Ethics Committee of the Stomatological Hospital of Chongqing Medical University. In this study, a heterotopic OS model was established using four-week-old female nude mice weighing 20 g. Fluorescently labeled

143 B cells (1×10^7 cells per site) were subcutaneously injected into the right hind limb of each mouse. When the tumor volume reached approximately 100 mm^3, the mice were randomly divided into four groups (n = 5): 1) control, 2) NIR II, 3) EARu, and 4) EARu + NIR II. EARu (100 μL, 1 mg/mL) was injected into the tumor margin, and the tumor site was irradiated with a 1064 nm infrared laser for 5 min. Infrared thermal imaging was employed to monitor real-time temperature changes and thermal mapping during treatment with two irradiations. The tumor volume and body weight of the mice were monitored every two days, and *in vivo* fluorescence imaging was performed on days 0, 3, 7, and 10 to assess the tumor size. Tumor Volume was calculated using a digital caliper according to the following formula: tumor volume = (tumor length) × (Width of Tumor)^2/2, corrected for volume folding. On day 10, the tumors were collected, sectioned, and stained with hematoxylin and eosin, Ki-67 antibody, and TUNEL assay. Additionally, major organs (heart, liver, spleen, lungs, and kidneys) were dissected and subjected to histological analysis using hematoxylin and eosin staining.

2.19. Cell adhesion

To observe cellular morphology, rBMSCs were seeded onto 3D-printed scaffolds and cultured for 3 d. Initially, the culture medium from each group was aspirated and the cells were washed twice with PBS. Subsequently, 4 % paraformaldehyde was added to fix the cells at 37 °C for 15 min, followed by two additional washes with PBS. For cellular permeabilization, 0.2 % TritonX-100 solution (Beyotime, Shanghai, China)was added and incubated at room temperature for 20 min, after which the cells were washed twice with PBS. Next, a 1:200 dilution of FITC-labeled phalloidin (Beyotime, Shanghai, China) was added to each well, and the cells were incubated in the dark at room temperature for 1 h. Upon completion of the incubation, the cells were washed twice with PBS, and the nuclei were stained with DAPI solution for 5 min. After two PBS washes, images were captured using a multifunctional fluorescence microscope.

2.20. ALP staining

rBMSCs were seeded onto 3D-printed scaffolds and induced with an osteogenic medium for 7 d. The osteogenic activity of the rBMSCs was determined by staining with a BCIP/NBT Alkaline Phosphatase Color Development Kit (Roche, Switzerland). After 30 min of staining, the solution was aspirated, and the cells were washed with PBS to terminate the color development reaction. Finally, the staining intensity in the plates was recorded using a camera, and microscopic images were captured using a multifunctional fluorescence microscope for further analysis.

2.21. Cranial defect in New Zealand rabbits

Eighteen male New Zealand rabbits, aged 8 weeks, were obtained from the Animal Experiment Center of Chongqing Medical University. The rabbits were randomly assigned to three groups (n = 3) for the construction of cranial defect models: 1) control, 2) BGC, and 3) EARu-BGC. Anesthesia was induced by the intravenous injection of pentobarbital sodium via the marginal ear vein, followed by a full-thickness skin incision on the cranial vault and periosteal stripping. Two defects, each with a diameter of 10 mm, were created on either side of the skull using a trephine. Scaffolds (Φ 10 × 10 × 2 mm^3) were then implanted into the defects, and the incisions were sutured. No adverse reactions were observed during the study period. At 4- and 8-weeks post-surgery, the rabbits were euthanized and their skulls were collected.

## 2.22. Micro-CT analysis of bone defects

The collected specimens were analyzed and reconstructed using a

micro-CT system (Bruker Corporation, Billerica, MA, USA). Quantitative analyses were performed to assess bone volume/tissue volume (BV/TV), trabecular separation (Tb.Sp), and trabecular number (Tb.N).

2.23. Hard tissue section preparation and histological staining

Following micro-CT examination, the dehydrated specimens were embedded in methyl methacrylate, and 30 μm thick sections were

prepared using a hard tissue cutting and grinding system (E200CP, EXAKT Verteriebs, Germany). To evaluate the newly formed bone tissue, the sections were stained with methylene blue-acid magenta and Masson's trichrome, and observations were made using an Olympus VS200 system.
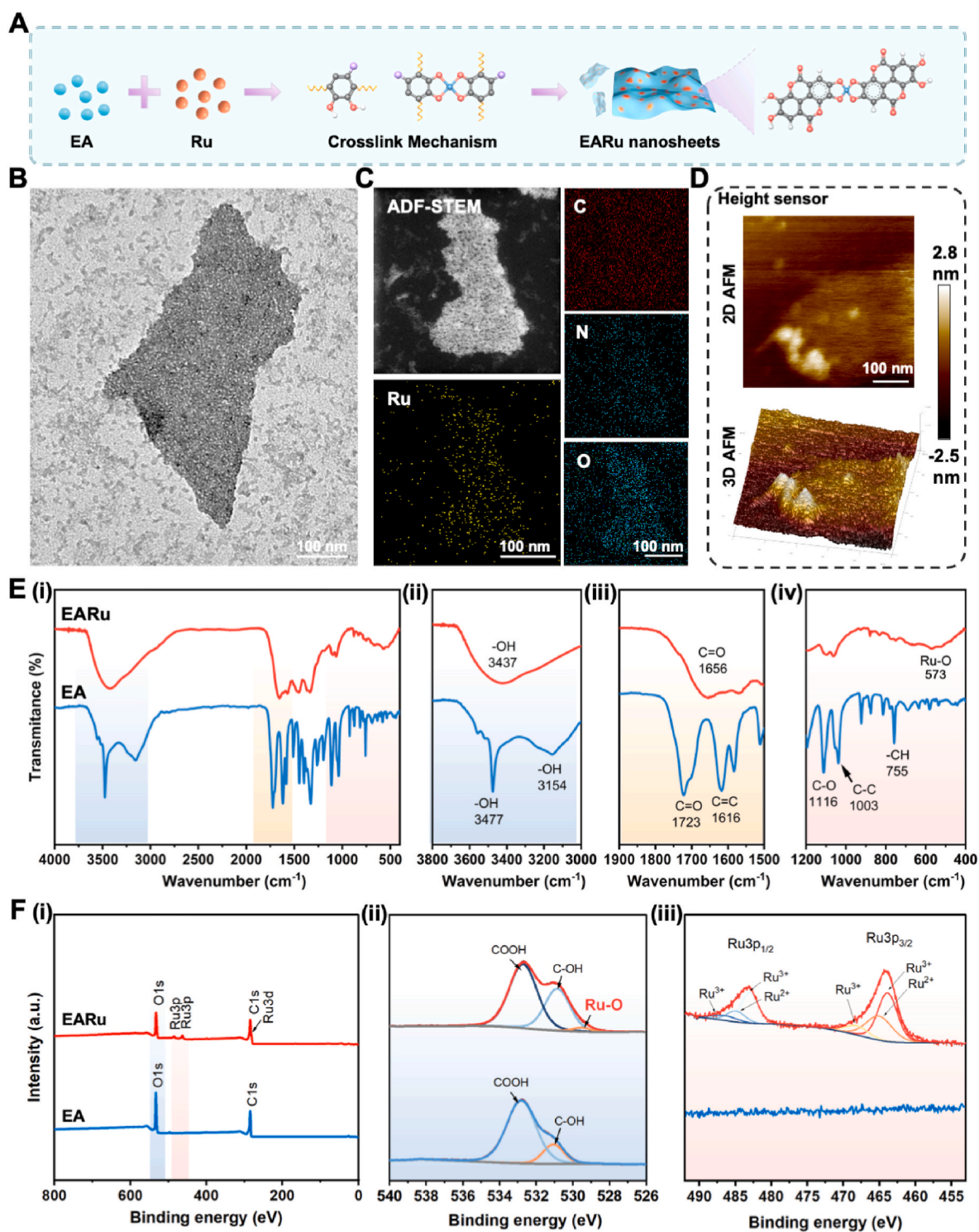
Fig. 2. Synthesis and characterization of EARu. A) Schematic of the synthesis of EARu. B) Representative TEM and C) ADF-STEM image of EARu, related element mapping (C, O, N, and Ru). D) 2D and 3D AFM image of EARu. E) FTIR spectra of EARu and EA. F) XPS spectra (i), high-resolution XPS spectra of the O1s peak (ii), and high-resolution XPS spectra of the Ru3p peak (iii) for EARu and EA.

2.24. Sequential fluorescent labeling

Based on previous studies, a multicolor sequential fluorescent labeling approach was employed to elucidate the processes of new bone formation and mineralization. Alizarin Red, tetracycline hydrochloride, and calcein (each at a dose of 30 mg/kg) were injected subcutaneously into the rabbit neck at 1-, 2-, and 3-weeks post-surgery, followed by additional injections at 2-, 4-, and 6-weeks post-surgery. Fluorescence was observed using a confocal microscope.

2.25. Statistical analysis

Data are presented as means $\pm$ standard deviation (n $\geq$ 3). All experiments were performed in triplicates. Prior to performing one-way analysis of variance (ANOVA), the assumptions of normality and homogeneity of variance were tested using the Shapiro-Wilk test and Levene's test, respectively. These tests confirmed that the data met the requirements for ANOVA. Multiple comparisons were assessed using GraphPad Prism 10.2.0, with the statistical significance level set at $p < 0.05$. The results are denoted as follows: ns indicates not significant, $*p < 0.05$, $**p < 0.01$, and $***p < 0.001$.

3. Results and discussion

3.1. Synthesis and characterization of EARu nanosheets

In this study, a strategy based on the MPN method was employed, where EA and Ru were coordinated to form 2D nanosheets (EARu). The detailed synthesis process is illustrated in Fig. 2A. During this process, EA and RuCl$_3$ reacted through the chelation of Ru ions with the catechol groups of EA, accompanied by covalent bonding between EA molecules, resulting in the formation of an organic-inorganic hybrid material with a unique structure. TEM images revealed that EARu exhibited a nanoscale sheet-like morphology with a width of approximately 100 nm and was relatively thin (Fig. 2B). EDS further confirmed the elemental distribution within the EARu, demonstrating that the characteristic elements EA (C, O, and N) and Ru were uniformly distributed across the nanosheets (Fig. 2C). AFM was employed to accurately assess EARu thickness. The results indicate that the EARu nanosheets reached a maximum thickness of approximately 5 nm, demonstrating a typical 2D layered structure, which suggests that the material possesses a high surface area and enhanced functional characteristic potential (Fig. 2D).

FTIR, XRD, and XPS were used to further characterize the structural and chemical bonding properties of the EARu. As shown in Fig. 2E, the FTIR spectrum revealed that within the wavenumber range of 3800–3000 cm^{-1}, EA exhibits two distinct absorption peaks at 3477 and 3154 cm^{-1}, whereas the EARu showed only one peak at 3437 cm^{-1}. This variation suggested the presence of –OH stretching vibrations, indicating the potential chelation reaction between EA and Ru. Furthermore, in the wavenumber range of 1900–1500 cm^{-1}, notable alterations in the C=O and C=C vibrational modes in EARu compared to EA implied a transformation of the carboxylic acid groups in EA to aromatic ester groups, thereby indicating the formation of possible covalent bonds between EA molecules. In the wavenumber range of 1200-400 cm^{-1}, the emergence of a new peak at 573 cm^{-1} in EARu suggested the formation of coordination bonds between metal and oxygen, while the multiple peaks observed in EA at 1116, 1003, and 755 cm^{-1} further corroborate this change. This new peak can be attributed to the characteristic vibrations of Ru-O bonds. The XRD results indicate that the cross-linking process in EARu leads to significant changes in the crystal structure, and the cross-linking of ruthenium ions disrupts the original crystal sequence of EA (Fig. S1). As shown in Fig. 2F, XPS analysis revealed that, compared to EA, EARu exhibited Ru3p and Ru3d peaks, confirming the presence of ruthenium within EARu. Furthermore, peak splitting analysis of the O1s signal in the 540-526 eV energy range revealed the characteristic features of a newly formed Ru-O bond in EARu. Notably,

in the 490–495 eV range, the peak splitting analysis of the Ru3p signal indicated that ruthenium in EARu exists in mixed oxidation states of Ru^{2+} and Ru^{3+}, thereby providing promising potential for the application of EARu in simulating redox enzyme reactions. The thermogravimetric analysis (TGA) results showed the thermal stability of EA, EA + Ru and EARu. Although there is a more significant weight loss at lower temperatures, which may be due to the unstable functional group structure, EARu exhibits higher thermal stability above 600 °C (Fig. S1).

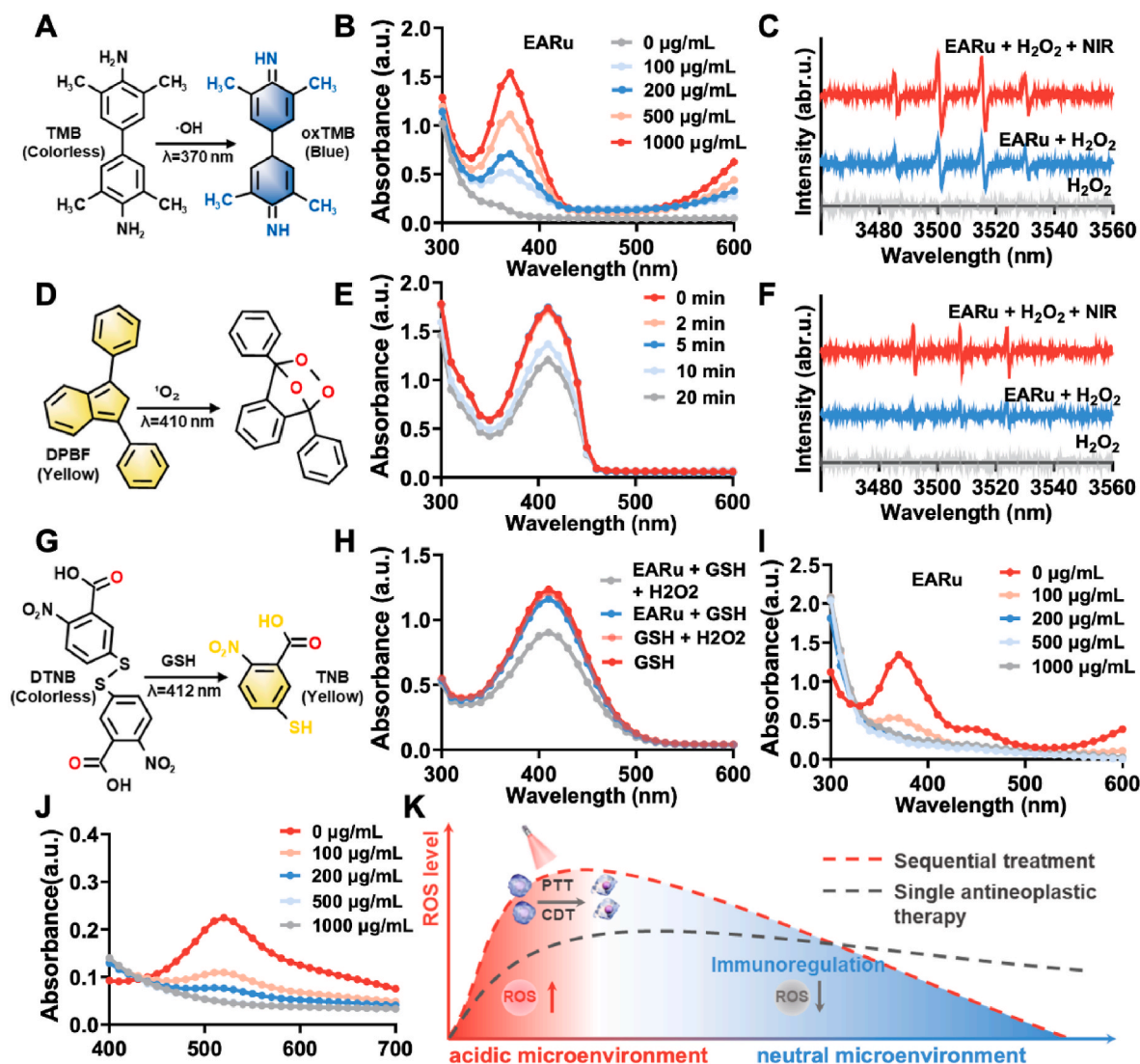*3.2. Chemodynamic performance of EARu*

The tumor microenvironment (TME) is a complex and dynamic physiological system composed of tumor cells, surrounding non-tumor cells, their components, and stroma. Notably, TME is characterized by acidic conditions, hypoxia, and elevated concentrations of H$_2$O$_2$ [34, 35]. These features provide unique therapeutic opportunities for CDT. Specifically, CDT leverages the acidic and H$_2$O$_2$-enriched conditions within the TME to catalyze reactions that generate highly reactive free radicals, selectively killing tumor cells while sparing normal tissues [36].

To assess whether EARu could induce tumor cell death through CDT, we evaluated its ability to generate ·OH and singlet oxygen (^{1}O$_2$) under an acidic and H$_2$O$_2$-rich condition, mimicking the TME. TMB was used as a probe for ·OH detection (Fig. 3A). When TMB and ·OH interact, the colorless TMB is oxidized and becomes blue [37]. Varying concentrations of EARu were added to solutions containing TMB and H$_2$O$_2$. After 10 min of reaction, the solution became bluer as the concentration of EARu increased. The absorbance peaks of the solutions were detected. As shown in Fig. 3B, the absorbance peak of oxidized TMB at 370 nm increased in a concentration-dependent manner in response to EARu. Similarly, at a fixed concentration of EARu, the absorbance peak at 370 nm increased proportionally with H$_2$O$_2$ concentration (Fig. S2). To detect ^{1}O$_2$, 1,3-diphenylisobenzofuran (DPBF) was used as the probe (Fig. 3D). ^{1}O$_2$ reacts with the conjugated double bonds of DPBF, causing a decrease in its absorbance at 410 nm [38]. The absorbance peak of DPBF at 410 nm decreased in a time-and EARu concentration-dependent manner (Fig. 3E and Fig. S3).

Additionally, the production of ·OH and ^{1}O$_2$ was confirmed qualitatively using ESR spectroscopy. For ·OH, no significant ESR signal was observed in the H$_2$O$_2$ group alone, while a characteristic four-line signal (1:2:2:1), corresponding to the DMPO-OH radical adduct, was detected in the EARu + H$_2$O$_2$ group, confirming the generation of ·OH (Fig. 3C). Similarly, the EARu + H$_2$O$_2$ group showed a characteristic three-line signal indicative of the TEMP-^{1}O$_2$ radical adduct, confirming the production of ^{1}O$_2$ (Fig. 3F). Notably, under NIR stimulation, both ·OH and ^{1}O$_2$ signals were significantly enhanced. This enhancement was likely owing to EARu absorbing NIR light and converting it into heat energy (Fig. S4), which increases the local temperature and accelerates the reaction, thereby promoting radical generation. Furthermore, EARu may promote electron transfer through the ligand-metal charge transfer effect under NIR stimulation, thereby accelerating the redox cycle of multivalent Ru ions [39,40]. This effect ensured the continuous progress of the Fenton-like reaction, thereby generating more free radicals. Meanwhile, 5,5′-dithiobis (2-nitrobenzoic acid) (DTNB), a frequently used indicator of GSH, turned yellow after reacting with GSH (Fig. 3G). As shown in Fig. 3H, compared with the other groups, the (EARu + GSH + H$_2$O$_2$) group indicated a significantly lower absorption peak at 412 nm, suggesting that the EARu-mediated catalytic reaction can deplete GSH. Therefore, EARu can effectively disrupt redox homeostasis in the tumor microenvironment.

However, tissue repair may be affected by ongoing free radical generation following tumor ablation [41]. Therefore, we explored the free radical-scavenging ability of EARu under neutral conditions to mimic the tissue repair microenvironment. TMB and DPPH were used to measure ·OH and reactive nitrogen (RNS), respectively. As shown in Fig. 3I, the EARu solution effectively scavenged the ·OH generated by

Fig. 3. Chemodynamic performance of EARu. A) Structural and color changes before and after the reaction of TMB with ·OH. B) Changes in TMB oxidation under acidic conditions with EARu concentrations indicates that EARu mediates ·OH generation. C) ESR spectra showing ·OH generation after different treatments. D) Structural and color changes before and after the interaction of DPBF with $^1O_2$. E) Time-dependent changes in DPBF under acidic conditions indicate that EARu mediates $^1O_2$ generation. F) ESR spectra showing the $^1O_2$ generation after different treatments. G) Structural and color changes before and after the interaction of DTNB with GSH. H) Absorbance curves changes in DTNB after different treatments. I) Absorbance curves changes of TMB with changes in EARu concentrations under neutral conditions (PH = 7.4). J) Absorbance curves changes in DPPH with changes in EARu concentrations under neutral conditions. K) Schematic of sequential treatment of antitumor and tissue remodeling mediated by EARu.

$FeSO_4$ and reduced the absorbance at the characteristic 370 nm. The scavenging of ·OH by EARu was concentration-dependent, and 500 μg/mL EARu reaction system could almost completely eliminate ·OH. Simultaneously, EARu also exhibited concentration-dependent RNS scavenging ability (Fig. 3J).

In summary, EARu exhibited switchable and controllable enzyme-mimicking activity, which can generate ·OH and $^1O_2$ in the acidic microenvironment of tumors, and scavenge excess ROS under neutral conditions. This switching effect matches the sequential treatment mode of OS, which tends to ablate tumors in the tumor ablation stage (acidic conditions) and promote tissue regeneration in the bone tissue repair phase (neutral conditions) (Fig. 3K).

3.3. Fabrication and characterization of EARu-BGC scaffolds

The trabecular microstructure of natural bone, characterized by an intricate 3D network, effectively facilitates vascular infiltration, cellular adhesion and proliferation [42]. This structure ensures an adequate nutrient supply and efficient removal of metabolic waste, thereby maintaining the functionality and health of the bone tissue [43,44]. Inspired by the trabecular architecture, we developed a 3D-printed bioceramic scaffold featuring biomimetic multiscale porous structures and interconnected channel networks designed to replicate the function of natural trabeculae and promote tissue regeneration and repair (Fig. 4A). The non-topology-dependent adhesion properties of EA catechol were utilized to immobilize EARu onto 3D-printed bioglass ceramic scaffolds to form a composite material named EARu-BGC. The main component of BGC is A-W bioglass ceramic, XRD results show that the AW bioglass powder is in an amorphous glass state before sintering, and obvious characteristic peaks of wollastonite and apatite can be seen after sintering. (Fig. S5). The chemical composition of AW is similar to the nominal composition of A-W bioglass ceramic (Table S1), consisting of approximately 33.2 % SiO_2, 15.1 % P_2O_5, 46.3 % CaO, and 4 % MgO. However, since XRF reports data in the form of oxides, the presence of CaF_2 cannot be confirmed, though it may still exist. During the synthesis of EARu, the BGC scaffold was immersed in the reaction solution to
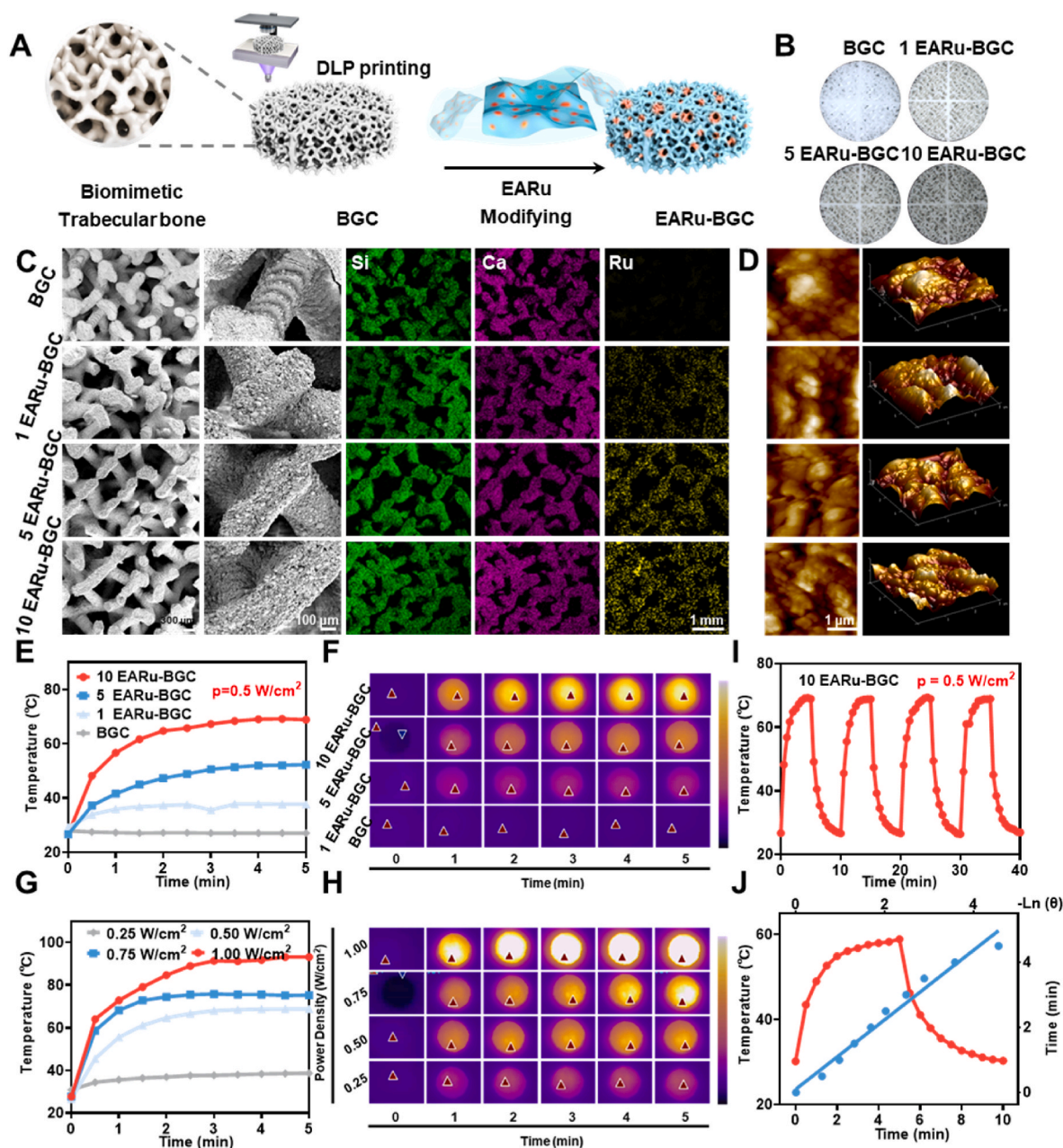
Fig. 4. Synthesis and photothermal properties of EARu-BGC scaffold. A) Schematic of the preparation of EARu scaffolds. B) Digital images of BGC scaffolds after 0, 1, 5, and 10 EARu deposition reactions. C) SEM images of BGC, 1 EARu-BGC, 5 EARu-BGC, and 10 EARu-BGC and corresponding elemental (Ru, Si, and Ca) mapping. D) AFM images of BGC, 1 EARu-BGC, 5 EARu-BGC, and 10 EARu-BGC. E) Heating curves and F) infrared images of BGC, 1 EARu-BGC, 5 EARu-BGC, and 10 EARu-BGC scaffolds under 1064 nm laser irradiation. G) Heating curves and H) infrared images of 10 EARu-BGC scaffolds under 1064 nm laser irradiation with different powers. I) Temperature cycling curves of 10 EARu-BGC scaffolds within 5 cycles of turning on and off the 1064 nm laser. J) Photothermal-heating curve and the corresponding calculation of the photothermal conversion efficiency between time and -lnθ.

deposit nanosheets and then dried at 60 °C for 30 min. This procedure was repeated one, five, and ten times to obtain the final EARu-BGC scaffolds, which were named 1 EARu-BGC, 5 EARu-BGC, and 10 EARu-BGC, respectively. Digital photographs showed that the obtained scaffold structure was well designed and staggered evenly, and the color of the scaffold gradually deepened with an increase in the number of reactions (Fig. 4B). The FTIR results showed that with the increase of EARu modification times (from 1 to 10 times), more obvious absorption peak fluctuations consistent with EARu appeared in the wavenumber range of 1900-1500 cm^{-1}.The XRD results demonstrate that increasing the number of EARu modifications on BGC leads to progressive changes in the crystalline structure. The TGA results also showed that as the

number of EARu modifications increased, the weight loss became more pronounced (Fig. S6). SEM images indicated that the BGC scaffold possessed well-defined macropores and a rough surface, with modification by EARu further increasing the surface roughness. Additionally, the elemental mapping images confirmed the uniform distribution of Si, Ca, and Ru across the scaffold, with the intensity of the Ru signal increasing with the number of deposition cycles (Fig. 4C and D). These results indicate that EARu was successfully integrated into the BGC scaffold. At the same time, the porosity and pore size of BGC, 1 EARu BGC, 5 EARu BGC, and 10 EARu BGC scaffolds were specified. The results showed that the porosity and average pore size of BGC were 70.84 ± 2.76 % and 0.36 ± 0.02 mm, respectively, while the modification of

EARu did not cause significant differences (Fig. S7).

Recent research indicates that the second near-infrared region (NIR-II, wavelength range of 1000–1700 nm) offers enhanced tissue penetration and elevated laser safety thresholds compared with the first near-infrared region (NIR-I, wavelength range of 700–900 nm) [45]. The attributes of NIR-II render it especially appropriate for PTT in OS, as it can efficiently penetrate deep tissues while substantially reducing possible harm to the surrounding healthy tissues [46]. Consequently, we conducted a detailed examination of the photothermal conversion efficiency of the EARu-BGC scaffold under NIR-II irradiation to evaluate its suitability for OS treatment. After 5 min of irradiation at 1064 nm with a power density of 0.5 W/cm^2, the pure BGC scaffold exhibited no significant temperature change, while the temperature of the 10 EARu-BGC scaffold increased to 66 °C, confirming the efficiency and rapidity of the scaffold's photothermal conversion (Fig. 4E and F). Furthermore, the photothermal effect was found to be dependent on the laser irradiation power density, with temperatures rising in correlation with increased power, ranging from 0.25 to 1 W/cm^2 (Fig. 4G and H). To assess the photothermal stability of the 10 EARu-BGC scaffolds, they were

subjected to five cycles of 1064 nm laser irradiation (laser irradiation for 5 min, followed by natural cooling to room temperature). The results demonstrated stable photothermal performance across the five "on-off" cycles, with no significant change in peak temperature. Under 1064 nm laser irradiation at 1 W/cm^2 (Fig. 4I). The photothermal conversion efficiency (PCE) of EARu reached an ultrahigh of 61.07 % (Fig. 4J), significantly surpassing that of most other reported NIR-II photothermal agents, such as NbSe$_2$ nanosheets (48.3 %) [47], FePS$_3$ nanosheets (43.3 %) [48], and bismuth-doped iron selenide nanoparticles (31.9 %) [49], highlighting its potential as an efficient NIR-II photothermal agent. The remarkable PCE and superior CDT capabilities of the EARu nanosheets, along with the biocompatibility and bone-regenerative qualities of the BGC scaffold, establish the EARu-BGC composite as a highly attractive candidate for OS treatment.

In addition, since the ion release ability of the scaffold largely determines its anti-tumor efficiency and later osteogenesis, the release kinetics of the EARu-BGC scaffold was studied. As shown in Fig. S7, the ion release rate of the EARu-BGC scaffold in an acidic environment (pH = 5.5) was faster than that in a neutral environment (pH = 7.4),
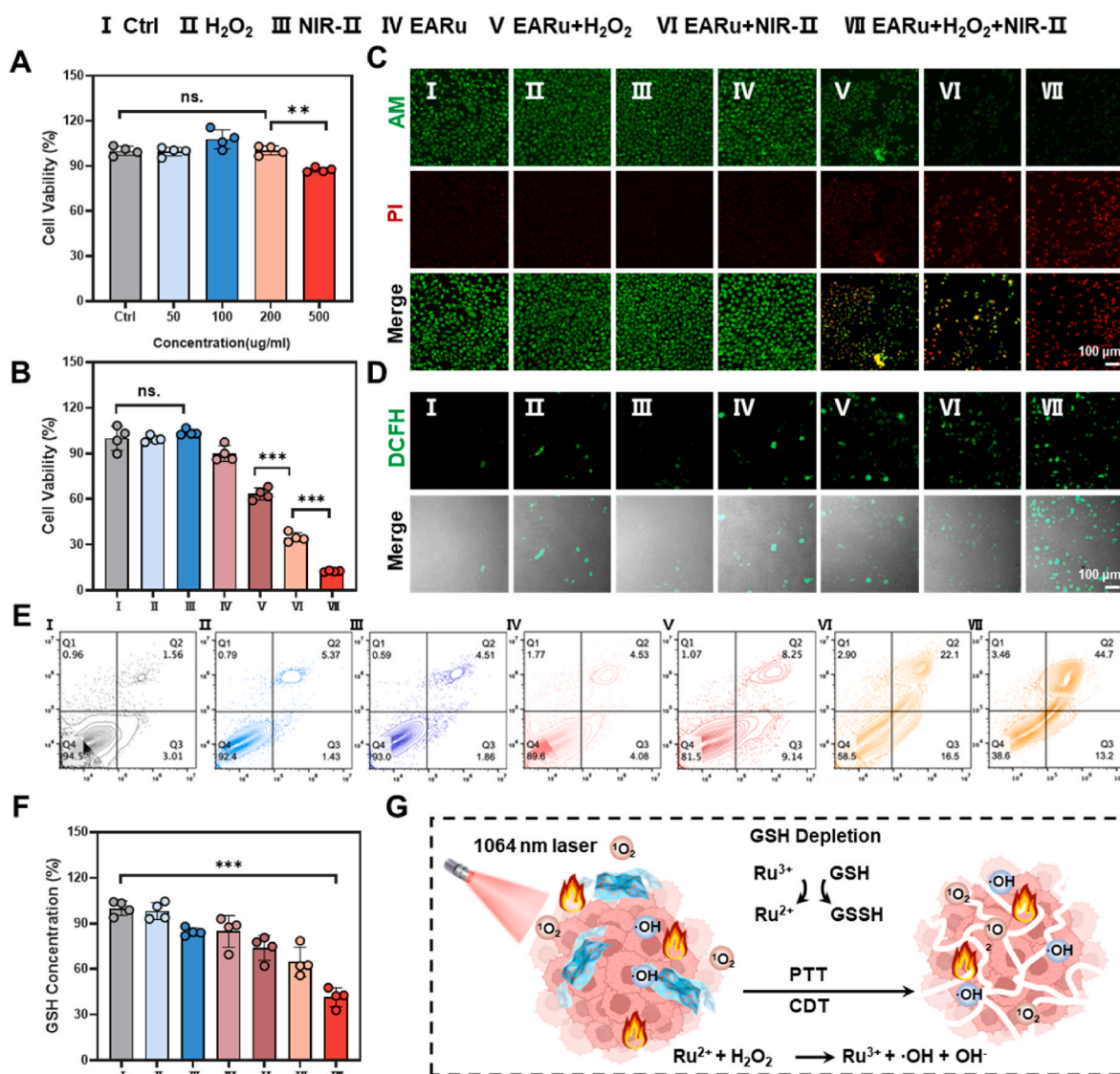
Fig. 5. EARu mediates tumor cell ablation *in vitro* through the mutual amplification effect of PTT and CDT. A) Relative survival rate of 143B cells incubated with different concentrations of EARu for 24 h. B) Relative survival rate of 143B cells after different treatments. C) Live-dead staining of 143B cells after different treatments. D) DCFH staining of 143B cells after different treatments. E) Flow cytometry analysis of apoptosis levels of 143B cells after different treatments. F) GSH content of 143B cells after different treatments. G) Diagram of the antitumor mechanism of EARu *in vitro*. EARu exerts antitumor effects through the synergistic amplification effect of PTT and CDT and GSH depletion. Error bar represent mean ± SD (≥3) ; *p < 0.05, **p < 0.01, ***p < 0.001.

confirming the sensitivity of the scaffold to the acidic tumor microenvironment. First, the acidic environment accelerated the disintegration of the metal-polyphenol network, allowing EARu-BGC to release Ru ions faster. On the other hand, in the bioglass scaffold, the hydrogen ions in the acidic environment interacted with the calcium-oxygen bonds, promoting the dissolution of Ca ions, while the silicon-oxygen network was relatively stable and the Si ions were stably released. In general, more Ru and Ca ions were released in the acidic microenvironment, which was conducive to enhancing tumor ablation, inducing tumor cell death and promoting later osteogenesis.

3.4. In vitro antitumor effect of EARu

The premise of EARu as a superior option for OS treatment lies in the absence of a significant killing effect on normal cells and its ability to selectively kill tumor cells. To validate this premise, we initially conducted a thorough investigation into the cytocompatibility of EARu with BMSC. The experimental results demonstrated that even at doses of up to
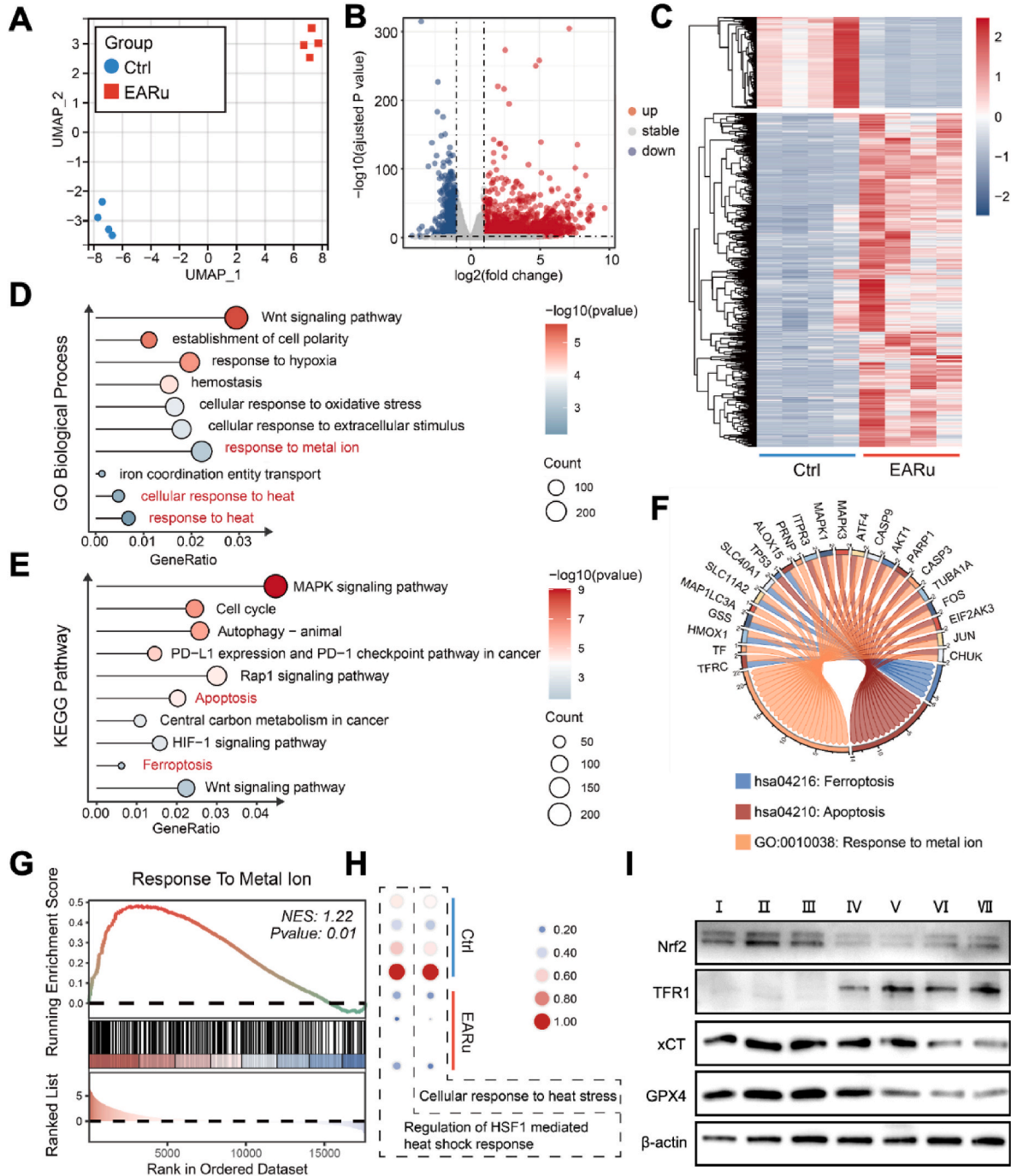
Fig. 6. Transcriptome analysis of 143B cells following EARu-mediated PTT and CDT synergistic therapy. A) UMAP analysis of 143B following EARu-mediated PTT and CDT synergistic therapy. B) Volcano plot showing the identified up/downregulated genes between EARu group versus Ctrl group. C) Heatmap of differentially expressed genes (DEGs) expression. D) Gene ontology (GO) enrichment analysis of biological process of DEGs. E) Kyoto Encyclopedia of Genes and Genomes (KEGG) enrichment analysis of DEGs. F) GSVA analysis results related to cellular response to heat. G) GSEA of response to metal ion. H) Circular visualization of the results of enrichment analysis. I) Western blot analysis of ferroptosis-related protein expression toward 143B cells after different treatments. I) Ctrl group, II) H$_2$O$_2$ group, III) NIR II group, IV) EARu group, V) EARu + NIR II group, VI) EARu + H$_2$O$_2$ group, and VII) EARu + H$_2$O$_2$ + NIR II group.

500 μg/mL, the cell survival rate remained at 90 % after 24 h of treatment, hence confirming the excellent biocompatibility of EARu (Fig. 5A). To further verify that EARu can kill tumor cells through the synergistic effect of PTT and CDT, 143 B cells were treated with NIR II and H_2O_2. As expected, H_2O_2, NIR-II, and EARu alone showed no obvious cytotoxicity. The survival rates of tumor cells for EARu + H_2O_2 and EARu + NIR II were 63.44 ± 3.91 % and 34.87 ± 3.08 %. However, under co-stimulation with the NIR-II laser and H_2O_2, EARu triggered >90 % ablation of 143 B cells, which was much better than single stimulation (Fig. 5B). In addition, cell live/death staining and apoptosis flow cytometry analyses corroborated these findings (Fig. 5C–E). The results showed that tumor cells were almost completely ablated under the co-stimulation of NIR-II and H_2O_2, thus validating the remarkable potential of EARu in the field of OS treatment via the synergistic effects of CDT and PTT. In addition, EARu-BGCs effectively induced apoptosis through photothermal ablation (Fig. S9).

To investigate the killing mechanism, we performed a 2,7-dichlorofluorescein diacetate (DCFH-DA, green) assay using CLSM to verify the generation of intracellular ROS. Compared to the control and NIR II groups, only the H_2O_2 group showed weak green fluorescence. In contrast, a strong green fluorescence was observed in cells incubated with EARu and H_2O_2, which was significantly enhanced under NIR-II laser irradiation (Fig. 5D). These results indicated that PTT-enhanced CDT produces a large amount of ROS, leading to cell death. Glutathione (GSH) is necessary for maintaining redox homeostasis in cancer cells. It directly removes ROS and alleviates oxidative stress through the cycle between the reduced form (GSH) and oxidized form (GSSG). Simultaneously, GSH binds to oxidative molecules to prevent oxidative damage to proteins, lipids, and DNA [50]. Among the treatment groups, the GSH content in the EARu + H_2O_2 + NIR II group was the lowest (only 41.47 ± 6.19 %). In contrast, in the presence of EARu + H_2O_2 and EARu + NIR II, the GSH content increased to 73.87 ± 8.16 % and 64.81 ± 9.67 %, respectively, demonstrating that EARu-mediated PTT synergizes with CDT to consume intracellular GSH and disrupt redox homeostasis in tumor cells (Fig. 5F and G).

3.5. Therapeutic mechanisms of EARu nanosheets

To further analyze the potential mechanism of EARu-mediated synergistic killing of OS, mRNA transcriptome analysis was performed to analyze the differences in gene expression. Treatment with EARu + H_2O_2 + NIRII significantly induced transcriptomic changes in the cells, which exhibited stable consistency and demonstrated good two-dimensional clustering in UMAP analysis (Fig. 6A). EARu treatment upregulated the expression of 2439 genes and downregulated the expression of 702 genes (Fig. 6B and C). We performed GO enrichment and KEGG pathway analyses of the differentially expressed genes. The CDT and PTT effects of EARu induced transcriptional changes in OS cells associated with ferroptosis and cellular responses to heat (Fig. 6D and E). The cellular heat response is a protective mechanism activated in response to high temperatures, and HSPs are representative functional proteins that help tumor cells resist the thermal effects of PTT. As shown in Fig. 6H, EARu significantly diminished the protective heat response of OS cells, potentially related to the interaction between Ru and HSPs, which has been the focus of existing studies exploring the use of Ru complexes to target HSPs in cancer therapy [51]. Simultaneously, the large amount of ROS generated by EARU-mediated CDT can inhibit the expression and function of HSPs.

Ferroptosis is an iron-dependent form of regulated cell death process. In the GO enrichment analysis, we observed an enrichment associated with iron coordination entity transport, which may be related to intracellular iron accumulation linked to ferroptosis. Furthermore, in the GSEA, we found that under the influence of EARu + H_2O_2 + NIR, 143B cells exhibited an activated state of responsiveness to metal ions, suggesting their potential involvement in apoptotic and ferroptotic processes of programmed cell death (Fig. 6F and G). We further detected

key molecules in multiple pathways that regulate ferroptosis, such as the cystine/glutamate antiporter SLC7A11 (also known as xCT), GPX4, and the transferrin receptor protein in the iron ion transport pathway 1 (TFR1). Compared to the control group, the expression levels of xCT and GPX4 were significantly downregulated and the expression of TFR1 was significantly upregulated in cells treated with EARu + H_2O_2+NIR II. However, no significant changes were found in the protein levels of xCT, GPX4 and TFR1 among the Ctrl group, H_2O_2 group, NIR II group, and EARu group (Fig. 6I). In addition, Nrf2 is an important transcription factor for cells to combat oxidative stress and plays a crucial role in cancer cell survival and treatment resistance by regulating downstream antioxidant genes to combat ferroptosis [52]. As shown in Fig. 6I, EARu-mediated PTT and CDT effect downregulated the expression of Nrf2. In summary, the synergistic effects of CDT and PTT led to pronounced modifications and promoted ferroptosis in tumor cells.

3.6. In vivo antitumor effects of EARu nanosheets

Given the promising tumor cell-killing effect of EARu *in vitro*, we further investigated its' *in vivo* antitumor effects in an ectopic OS mouse model. First, we constructed a 143 B cell tumor mouse model expressing luciferase (143B-luc). Using bioluminescence imaging, tumor volume monitoring, and histological staining, we evaluated the antitumor activity and potential mechanisms of EARu under different treatment conditions (Fig. 7A).

After EARu was injected locally into the tumor, irradiation was performed with a laser at a wavelength of 1064 nm and power of 1.0 W/cm^2 and the temperature was recorded in real time using an infrared imaging camera. As shown in Fig. 7C and D, the tumor temperature in the EARu + NIR II group rapidly increased from 33.7 °C to 53.2 °C within 5 min, while the temperature change in the NIR group was negligible, indicating that EARu still has excellent photothermal conversion ability when applied *in vivo*. Bioluminescence imaging was used to noninvasively monitor the degree of tumor infiltration and the number of tumor cells, and the results showed that in the EARu + NIR II group, the tumor fluorescence signal almost completely disappeared after two treatments (Fig. 7B). Moreover, regular monitoring of the tumor volume showed that EARu combined with NIR II irradiation significantly inhibited tumor growth and ultimately eradicated the tumors within 10 days, whereas the tumor volume in the other treatment groups increased rapidly (Fig. 7E and F). This was supported by the tumor weights (Fig. 7G) and images of the excised tumors (Fig. 7H), demonstrating similar results. Notably, despite the significant antitumor effect of EARu, the body weight of the mice did not change significantly during the treatment period, suggesting that the systemic toxicity of EARu was low (Fig. S10). H&E staining experiments further confirmed the low cytotoxicity of EARu, and histological changes in the major organs of mice were not obvious (Fig. S11). These results not only provide strong support for the clinical application of EARu but also lay a solid foundation for its wide application in the field of tumor therapy.

To further validate the antitumor mechanism of the combined treatment with EARu and NIR-II, we employed H&E, Ki67, and TUNEL staining to assess cell proliferation and apoptosis at the tumor sites (Fig. 7I). As shown in the H&E-staining image, the EARu + NIR II group exhibited significantly enlarged intercellular spaces along with nuclear shrinkage, implying severe damage to the tumors after photothermal tumor ablation. Ki67, a nuclear antigen, is a direct marker of cell proliferation. Both the control and NIR II groups exhibited significant Ki67-positive staining in tumor cells, indicating high proliferative activity. In contrast, the number of Ki67-positive cells decreased in the EARu treatment group, whereas a marked reduction was observed in the EARu + NIR-II group, indicating that combined treatment with EARu and NIR-II significantly inhibited the proliferative activity of tumor cells. Consistent with the Ki67 staining results, the EARu + NIR-II group displayed the strongest TUNEL-positive signal, demonstrating a pronounced apoptotic response in the tumor cells. In summary, under NIRII
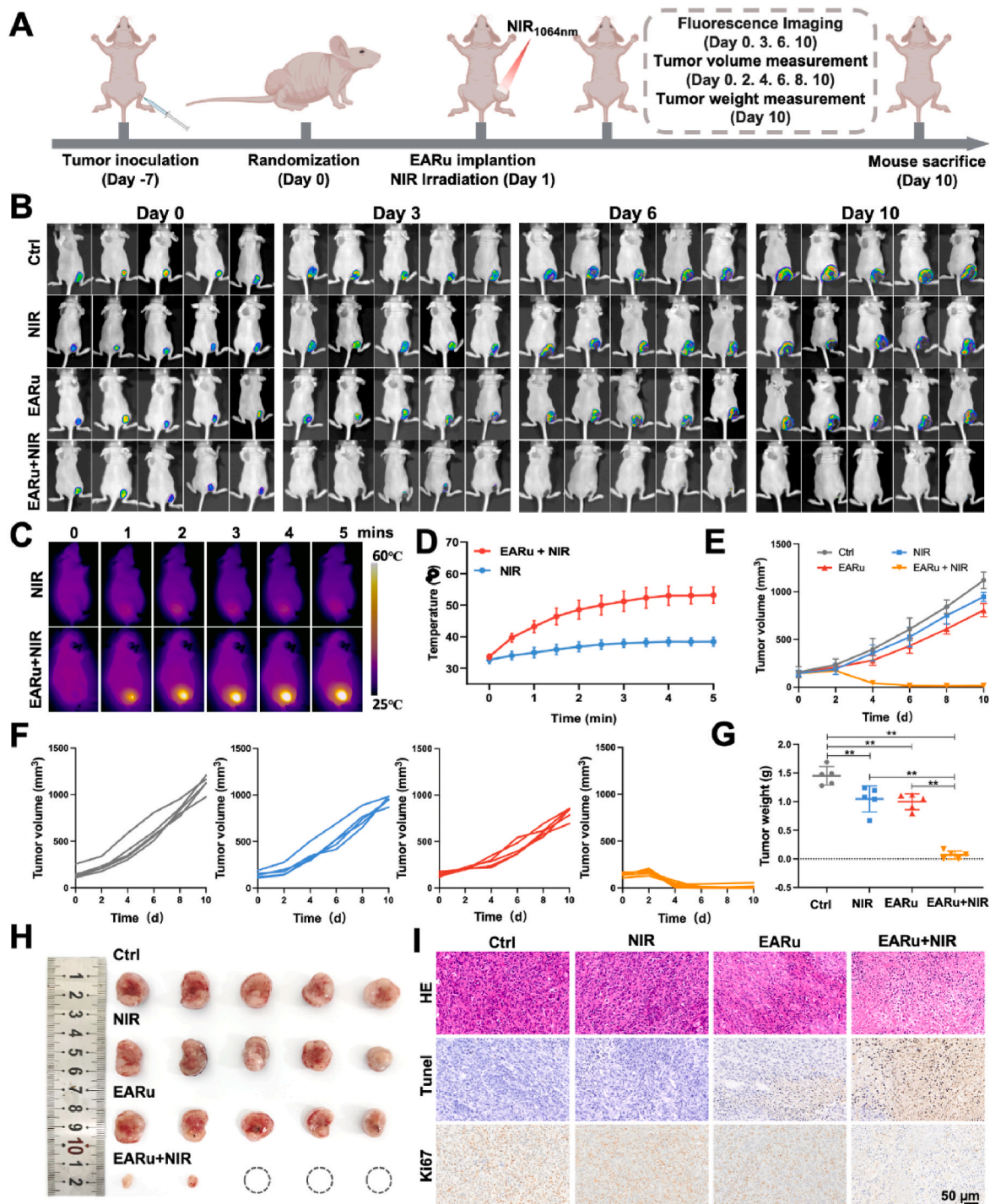
Fig. 7. *In vivo* antitumor effect of EARu. A) Schematic flow chart of *in vivo* antitumor effect. B) Bioluminescent images of 143B tumor-bearing mice before, during and after different treatments. C). Infrared thermal imaging of the tumor site of 143B tumor-bearing mice after different treatments under 1064 nm laser irradiation. D) Real-time temperature rise curve of 143B tumor-bearing mice after different treatments under 1064 nm laser irradiation. E) Tumor growth curves of the tumor-bearing mice measured by a caliber (n = 5). F) Individual tumor growth of tumor-bearing mouse in each group. G) Weights of resected tumors of 143B tumor-bearing mice after different treatments. H) Photos of resected tumors of 143B tumor-bearing mice after various treatments, with dotted circles indicating that the tumors have been eradicated. I) Representative images of H&E and immunohistochemical staining (TUNEL and Ki67) of tumor sections with different treatments. Error bar represent mean ± SD (≥3) ; *p < 0.05, **p < 0.01, ***p < 0.001.

irradiation, EARu, in conjunction with CDT and PTT, exerted superior antitumor activity by inhibiting tumor cell proliferation and inducing apoptosis.

3.7. In vitro and in vivo bone regeneration by EARu-BGC scaffolds

Considering the potential for adverse inflammatory responses in healthy tissues surrounding tumors owing to the effects of PTT and CDT, we evaluated the anti-inflammatory properties of EARu on macrophages in a neutral environment. The results demonstrated that EARu

significantly reduced the ROS levels in macrophages under inflammatory conditions in a dose-dependent manner. Immunofluorescence analysis indicated that EARu decreased iNOS expression while upregulating CD206, suggesting inhibition of M1 macrophage polarization and promotion of the M2 phenotype. PCR analysis further confirmed these findings, showing that EARu upregulated Arg *1* expression while downregulating *TNF-α* and *IL-6* (Fig. S12). Collectively, these results indicate that EARu effectively controls local inflammatory responses following tumor ablation, thereby promoting tissue repair.

Next, we investigated the osteogenic potential of EARu-BGC to assess its suitability for repairing bone defects following tumor ablation

(Fig. 8A). rBMSCs were seeded onto the EARu-BGC scaffold, and cell adhesion was evaluated using cytoskeletal staining. The results demonstrate that the cells were evenly distributed on the surface of the BGC scaffold and exhibited strong adhesion (Fig. 8B). Cytoskeletal fibers were clearly visible, and the cells displayed a stretched morphology with an intact cytoskeletal structure. Similarly, 1 EARu-BGC and 5 EARu-BGC exhibited comparable cell adhesion, whereas the cells on 10 EARu-BGC showed irregular morphology, with some failing to fully stretch, indicating poor adhesion. This suggests that as the number of EARu deposits increased, the cell response to the scaffold became more negative, likely owing to the increased coating thickness and cytotoxicity. These
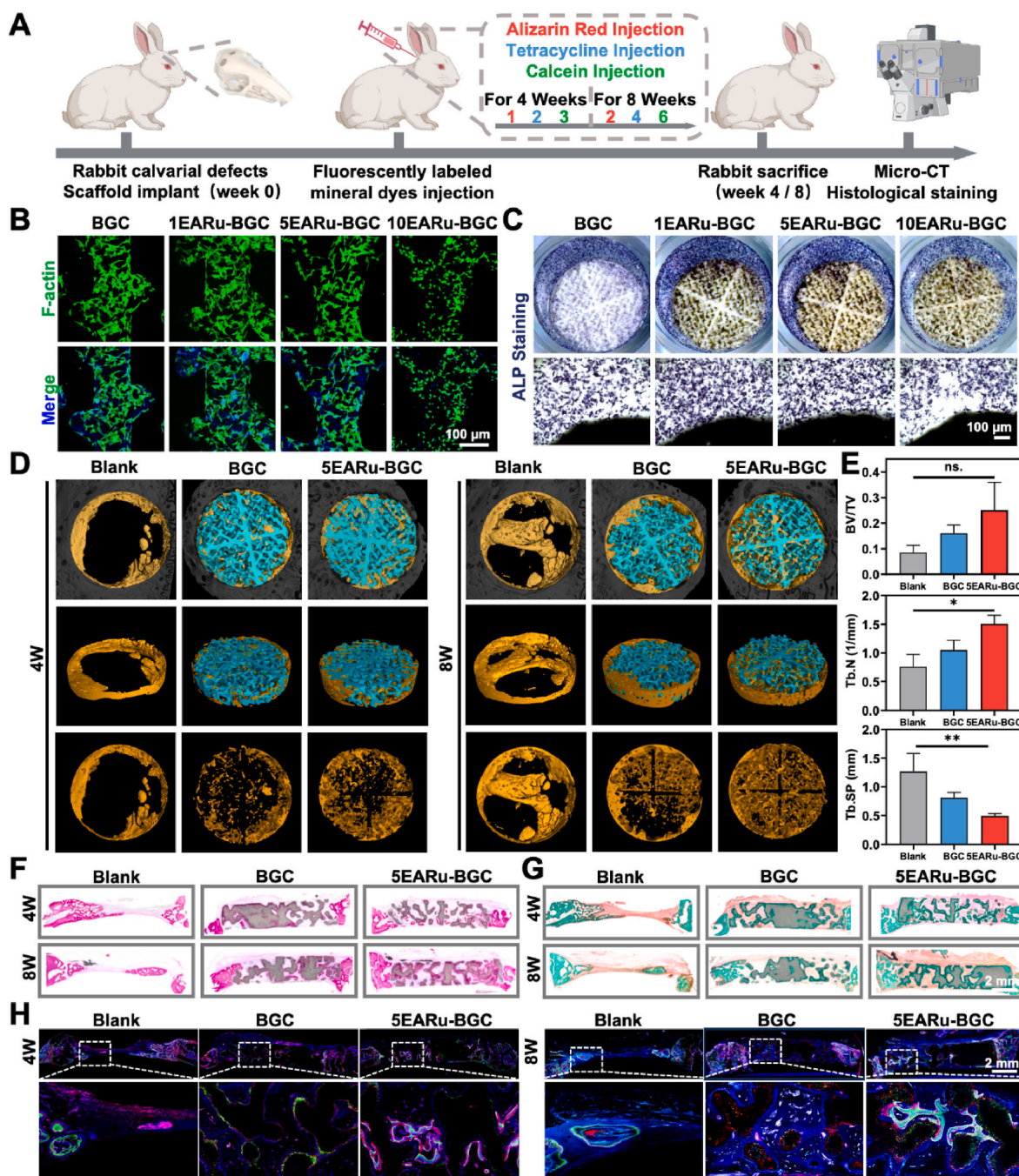
Fig. 8. Evaluation of the osteogenic bioactivity of EARu-BGC *in vitro* and *in vivo*. A) Flowchart of *in vivo* osteogenic assay in rabbits. B) Fluorescence staining of the cytoskeleton of rBMSCs adhered to different BGC scaffolds. C) ALP staining of rBMSCs cultured on different scaffolds after 7 d. D) Micro-CT 3D reconstruction images of cranial bone defects at 4 and 8 weeks after scaffold implantation. E) Quantification of BV/TV, Tb.N, and Tb.Sp of the defects. F) VG staining and G) Masson staining of rabbit cranial bone defects harvested at 4 and 8 weeks and implanted with ordinary BGC and EARu-BGC scaffolds. H) Sequential fluorescent labeling observation of new bone tissues of rabbit cranial bone defects harvested at 4 and 8 weeks. Error bar represent mean ± SD (≥3) ; *$p < 0.05$, **$p < 0.01$, ***$p < 0.001$.

findings were further supported by Alkaline phosphatase (ALP) staining. ALP, a key enzyme involved in early osteogenic differentiation, serves as a marker of cell function and osteogenic activity. EARu exhibited a concentration-dependent enhancement of ALP expression (Fig. S13). Compared to the BGC scaffold, one EARu-BGC and five EARu-BGC scaffolds showed significantly higher ALP expression (Fig. 8C). Previous studies have established that the macroporous structure of 3D-printed BGC scaffolds, along with the interconnection of elements such as Ca, Si, and P, effectively supports rBMSC attachment, proliferation, and osteogenic differentiation. Additionally, ellagic acid, a natural polyphenolic compound, promotes osteogenic differentiation by activating the SMAD2/3 signaling pathway [53,54]. Therefore, EARu-BGCs hold considerable promise for the repair of bone defects after OS ablation.

In *in vivo* studies, 5 EARu-BGC was selected to repair the cranial bone defects in New Zealand rabbits. The results demonstrated that EARu-BGC significantly enhanced new bone formation compared to the blank control and BGC scaffold groups. Specifically, the EARu-BGC group exhibited a greater volume of new bone nearly fully covering the defect area (Fig. 8D). Bone mass analysis revealed that the functionalized scaffold group exhibited a higher bone volume fraction (BV/TV), increased trabecular number (Tb.N), and reduced trabecular separation (Tb.Sp). These findings were corroborated by histological staining (Fig. 8E). Methylene blue acid magenta staining indicated denser new bone tissue and an intact trabecular structure in the functionalized scaffold group, suggesting more mature bone formation (Fig. 8F). Additionally, Masson's staining revealed a significant increase in collagen fiber content and uniform collagen deposition, indicating that matrix formation and mineralization in the new bone were markedly improved (Fig. 8G).

To further investigate the spatiotemporal dynamics of bone regeneration, a series of fluorescent mineral dyes was administered subcutaneously at predetermined intervals. New bone was labeled with alizarin red (red), tetracycline hydrochloride (blue), and calcein AM (green), with each color representing a different stage of osteogenesis. At both 4 and 8 weeks, the fluorescence intensity of EARu-BGC was significantly higher than that of the BGC, suggesting that EARu-BGC stimulates osteogenic activity more effectively. Furthermore, compared to the blank group, in which fluorescence was confined to osteogenesis around the defect margin, both BGC and EARu-BGC demonstrated new bone tissue attachment at the scaffold in the defect center, with the EARu-BGC signal being notably stronger (Fig. 8H). These findings confirmed that EARu-BGCs exhibited superior performance in promoting bone defect repair and demonstrated excellent bone regeneration potential.

4. Conclusions

This study addressed two significant challenges in the treatment of OS: the high recurrence rate post-surgery and the complex reconstruction of extensive bone defects. To solve such issues, we developed an 2D EARu nanosheet-modified BGC scaffold, a novel strategy not previously reported in the literature. This modified scaffold demonstrated exceptional adaptability to the tumor microenvironment, exhibiting enzyme-mimetic activities that dynamically shift in response to different therapeutic phases, thereby enabling a sequential treatment approach for tumor ablation and bone regeneration. During the tumor ablation phase, the EARu nanosheets demonstrated superior PTT and enhanced CDT under NIR-II irradiation. The synergistic effects of PTT and CDT significantly increased ROS production and depleted GSH, thereby triggering a lipid peroxidation cascade that effectively induces ferroptosis in tumor cells. In the subsequent bone-repair phase, the enzyme-mimetic properties of EARu nanosheets shifted to an antioxidative function, scavenging excess ROS, and promoting the anti-inflammatory polarization of macrophages. This transformation reprogrammed the microenvironment from a pathological state detrimental to tissue repair into one conducive to healing. Furthermore, the BGC scaffold was designed with

biomimetic porosity, inspired by the microstructural features of natural trabecular bone. Its customizable structure ensured seamless integration with the patient's native bone, while also providing an optimized framework for new bone formation. The controlled degradation of the BGC scaffold released mineral components essential for osteogenesis, including calcium, silicon, and phosphorus, which accelerated the repair of bone defects. In conclusion, the EARu-BGC scaffold successfully integrates antitumor and bone-repair functions into a single platform, making it a promising candidate for OS treatment. This study provides valuable insights into the application of 3D-printed BGC in bone tissue engineering and offer a reference for future research in the field. However, further studies are required to evaluate their clinical efficacy and safety.

CRediT authorship contribution statement

Guangyu Jian: Writing – original draft, Visualization, Validation, Methodology, Investigation, Formal analysis, Conceptualization. **Si Wang:** Resources, Methodology, Investigation, Formal analysis. **Xinlu Wang:** Writing – review & editing, Investigation. **Qinyi Lu:** Resources, Methodology, Formal analysis. **Xingyu Zhu:** Resources, Methodology. **Shucheng Wan:** Resources, Methodology. **Shan Wang:** Validation, Software. **Dize Li:** Validation, Software. **Chao Wang:** Resources, Methodology. **Qingqing He:** Writing – review & editing, Visualization, Validation, Investigation, Data curation. **Tao Chen:** Writing – review & editing, Supervision, Project administration, Funding acquisition, Conceptualization. **Jinlin Song:** Writing – review & editing, Supervision, Project administration, Funding acquisition, Conceptualization.

Ethics approval and consent to participate

All animal experiments and care were carried out in accordance with the ARRIVE guidelines, and were approved by the Animal Experiment Ethics Committee of the Stomatological Hospital of Chongqing Medical University (approval number: 2024-023).

Declaration of competing interest

The authors declare that they have no known competing financial interests or personal relationships that could have appeared to influence the work reported in this paper.

Appendix A. Supplementary data

Supplementary data to this article can be found online at https://doi.org/10.1016/j.bioactmat.2025.04.029.

References

[1] J. Gill, R. Gorlick, Advancing therapy for osteosarcoma, Nat. Rev. Clin. Oncol. 18 (10) (2021) 609–624.
[2] P.S. Meltzer, L.J. Helman, N. Engl. J. Med. 385 (22) (2021) 2066–2076.
[3] H.C. Beird, S.S. Bielack, A.M. Flanagan, J. Gill, D. Heymann, K.A. Janeway, J. A. Livingston, R.D. Roberts, S.J. Strauss, R. Gorlick, Osteosarcoma, Nat. Rev. Dis. Primers 8 (1) (2022) 77.
[4] S.N. Yu, X.D. Yao, Advances on immunotherapy for osteosarcoma, Mol. Cancer 23 (1) (2024) 192.

[5] M.S. Isakoff, S.S. Bielack, P. Meltzer, R. Gorlick, Osteosarcoma: current treatment and a collaborative pathway to success, J. Clin. Oncol. 33 (27) (2015) 3029–3035.

[6] J.S. Whelan, L.E. Davis, Osteosarcoma, chondrosarcoma, and chordoma, J. Clin. Oncol. 36 (2) (2018) 188–193.

[7] J. Ritter, S.S. Bielack, Osteosarcoma, vol. 21, Ann Oncol, 2010, pp. 320–325.

[8] C.R. Li, W. Zhang, Y.Y. Nie, X.F. Du, C.S. Huang, L. Li, J. Long, X.L. Wang, W. X. Tong, L. Qin, Y.X. Lai, Time-sequential and multi-functional 3D printed MgO$_2$/PLGA scaffold developed as a novel biodegradable and bioactive bone substitute for challenging postsurgical osteosarcoma treatment, Adv Mater. 36 (34) (2024) e2308875.

[9] C. Xu, Y.H. Xia, P.Z. Zhuang, W.L. Liu, C.P. Mu, Z.Y. Liu, J.L. Wang, L.L. Chen, H. L. Dai, Z.Q. Luo, FePSe$_3$-Nanosheets-Integrated cryogenic-3D-printed multifunctional calcium phosphate scaffolds for synergistic therapy of osteosarcoma, Small 19 (33) (2023) e2303636.

[10] G. Lei, L. Zhuang, B.Y. Gan, Targeting ferroptosis as a vulnerability in cancer, Nat. Rev. Cancer 22 (7) (2022) 381–396.

[11] W.S. Yang, R. SriRamaratnam, M.E. Welsch, K. Shimada, R. Skouta, V. S. Viswanathan, J.H. Cheah, P.A. Clemons, A.F. Shamji, C.B. Clish, L.M. Brown, A. W. Girotti, V.W. Cornish, S.L. Schreiber, B.R. Stockwell, Regulation of ferroptotic cancer cell death by GPX4, Cell 156 (1–2) (2014) 317–331.

[12] S.J. Dixon, K.M. Lemberg, M.R. Lamprecht, R. Skouta, E.M. Zaitsev, C.E. Gleason, D.N. Patel, A.J. Bauer, A.M. Cantley, W.S. Yang, B. Morrison, B.R. Stockwell, Ferroptosis: an iron-dependent form of nonapoptotic cell death, Cell 149 (5) (2012) 1060–1072.

[13] Y.M. Wang, X.R. Wu, Z. Ren, Y.L. Li, W.L. Zou, J.C. Chen, H.Q. Wang, Overcoming cancer chemotherapy resistance by the induction of ferroptosis, Drug Resist Updat 66 (2023) 100916.

[14] C. Zhang, X.Y. Liu, S.D. Jin, Y. Chen, R.H. Guo, Ferroptosis in cancer therapy: a novel approach to reversing drug resistance, Mol. Cancer 21 (1) (2022) 47.

[15] Q. Zhou, Y. Meng, D.S. Li, L. Yao, J.Y. Le, Y.H. Liu, Y.M. Sun, F.R. Zeng, X. Chen, G. T. Deng, Ferroptosis in cancer: from molecular mechanisms to therapeutic strategies, Signal Transduct Target Ther 9 (1) (2024) 55.

[16] W.T. Gao, X.Y. Wang, Y. Zhou, X.Q. Wang, Y. Yu, Autophagy, ferroptosis, pyroptosis, and necroptosis in tumor immunotherapy, Signal Transduct Target Ther 7 (1) (2022) 196.

[17] N. Singh, D. Kim, S. Min, E. Kim, S. Kim, Y.S. Zhang, H. Kang, J.S. Kim, Multimodal synergistic ferroptosis cancer therapy, Coordin Chem Rev 522 (2025) 216–236.

[18] P.R. Zhao, H.Y. Li, W.B. Bu, A forward vision for chemodynamic therapy: issues and opportunities, Angew Chem Int Ed Engl. 62 (7) (2023) e202210415.

[19] Y.F. Zhou, S.Y. Fan, L.L. Feng, X.L. Huang, X.Y. Chen, Manipulating intratumoral Fenton chemistry for enhanced chemodynamic and chemodynamic-synergized multimodal therapy, Adv Mater 33 (48) (2021) e2104223.

[20] S.L. Li, P. Jiang, F.L. Jiang, Y. Liu, Recent advances in nanomaterial-based nanoplatforms for chemodynamic cancer therapy, Adv. Funct. Mater. 31 (22) (2021) 2100243.

[21] D.Q. Sun, X.X. Sun, X. Zhang, J.P. Wu, X.B. Shi, J. Sun, C. Luo, Z.G. He, S.W. Zhang, Emerging chemodynamic nanotherapeutics for cancer treatment, Adv Healthc Mater 13 (22) (2024) e2400809.

[22] L.H. Fu, Y.L. Wan, C. Qi, J. He, C.Y. Li, C. Yang, H. Xu, J. Lin, P. Huang, Nanocatalytic theranostics with glutathione depletion and enhanced reactive oxygen species generation for efficient cancer therapy, Adv Mater 33 (7) (2021) e2006892.

[23] X.S. Li, J.F. Lovell, J. Yoon, X.Y. Chen, Clinical development and potential of photothermal and photodynamic therapies for cancer, Nat. Rev. Clin. Oncol. 17 (11) (2020) 657–674.

[24] Y. Fang, Y. Yu, X.Y. Jiang, P.L. Liu, Y. Chen, W. Feng, Self-adaptive MoO$_{3-x}$ subnanometric wires incorporated scaffolds for osteosarcoma therapy and bone regeneration, Adv. Funct. Mater. 33 (49) (2023) 2304163.

[25] S.T. Wu, M.T. Gao, L. Chen, Y.H. Wang, X.C. Zheng, B.Y. Zhang, J. Li, X.D. Zhang, R. Dai, Z.L. Zheng, R.P. Zhang, A multifunctional nanoreactor-induced dual inhibition of HSP70 strategy for enhancing mild photothermal/chemodynamic synergistic tumor therapy, Adv Healthc Mater 13 (23) (2024) 2400819.

[26] L.Y. Wang, Q.H. Yang, M.F. Huo, D. Lu, Y.S. Gao, Y. Chen, H.X. Xu, Engineering single-atomic iron-catalyst-integrated 3D-printed bioscaffolds for osteosarcoma destruction with antibacterial and bone defect regeneration bioactivity, Adv Mater. 33 (31) (2021) 2100150.

[27] J.H. Yin, S.S. Pan, X. Guo, Y.S. Gao, D.Y. Zhu, Q.H. Yang, J.J. Gao, C.Q. Zhang, Y. Chen, Nb$_2$C MXene-functionalized scaffolds enables osteosarcoma phototherapy and angiogenesis/osteogenesis of bone defects, Nano-Micro Lett. 13 (1) (2021) 30.

[28] Y.L. Zhang, L.G. Xia, D. Zhai, M.C. Shi, Y.X. Luo, C. Feng, B. Fang, J.B. Yin, J. Chang, C.T. Wu, Mesoporous bioactive glass nanolayer-functionalized 3D-printed scaffolds for accelerating osteogenesis and angiogenesis, Nanoscale 7 (45) (2015) 19207–19221.

[29] Y.L. Zhu, X.R. Zhang, G.Z. Chang, S. Deng, H.F. Chan, Bioactive glass in tissue regeneration: unveiling recent advances in regenerative strategies and applications, Adv Mater 37 (2) (2024) 2312964.

[30] S.S. Pan, J.H. Yin, L.D. Yu, C.Q. Zhang, Y.F. Zhu, Y.S. Gao, Y. Chen, 2D MXene-integrated 3D-printing scaffolds for augmented osteosarcoma phototherapy and accelerated tissue reconstruction, Adv Sci. 7 (2) (2020) 1901511.

[31] M.N. Gómez-Cerezo, D. Lozano, D. Arcos, M. Vallet-Regí, C. Vaquette, The effect of biomimetic mineralization of 3D-printed mesoporous bioglass scaffolds on physical

[32] H.L. Lu, Z.H. Li, Z.W. Duan, Y.X. Liao, K.Y. Liu, Y.W. Zhang, L. Fan, T.Y. Xu, D. Yang, S. Wang, Y.S. Fu, H.J. Xiang, Y. Chen, G.D. Li, Photothermal catalytic reduction and bone tissue engineering towards a three-in-one therapy strategy for osteosarcoma, Adv Mater. 36 (40) (2024) 2408016.

[33] M.P. Nikolova, M.S. Chavali, Recent advances in biomaterials for 3D scaffolds: a review, Bioact. Mater. 4 (2019) 271–292.

[34] Z.Y. Chu, J. Yang, W. Zheng, J.W. Sun, W.N. Wang, H.S. Qian, Recent advances on modulation of H2O2 in tumor microenvironment for enhanced cancer therapeutic efficacy, Coord. Chem. Rev. 481 (15) (2023) 215049.

[35] Y.L. Dai, C. Xu, X.L. Sun, X.Y. Chen, Nanoparticle design strategies for enhanced anticancer therapy by exploiting the tumour microenvironment, Chem. Soc. Rev. 46 (12) (2017) 3830–3852.

[36] W.T. Chen, J.X. Liu, C.Y. Zheng, Q. Bai, Q. Gao, Y.N. Zhang, K. Dong, T.L. Lu, Research progress on improving the efficiency of CDT by exacerbating tumor acidification, Int. J. Nanomed. 17 (2022) 2611–2628.

[37] X. Chen, Q.Q. He, Q.M. Zhai, H. Tang, D.Z. Li, X.Y. Zhu, X.H. Zheng, G.Y. Jian, R. D. Cannon, L. Mei, S. Wang, P. Ji, J.L. Song, T. Chen, Adaptive nanoparticle-mediated modulation of mitochondrial homeostasis and inflammation to enhance infected bone defect healing, ACS Nano 17 (22) (2023) 22960–22978.

[38] M. Liu, L. Huang, X.Y. Xu, X.M. Wei, X.F. Yang, X.L. Li, B.N. Wang, Y. Xu, L.H. Li, Z. M. Yang, Copper doped carbon dots for addressing bacterial biofilm formation, wound infection, and tooth staining, ACS Nano 16 (6) (2022) 9479–9497.

[39] Y. Chen, X.R. Yang, K. Li, J.K. Feng, X.Y. Liu, Y.X. Li, K.Y. Yang, J.H. Li, S.H. Ge, Phenolic ligand-metal charge transfer induced copper nanozyme with reactive oxygen species-scavenging ability for chronic wound healing, ACS Nano 18 (9) (2024) 7024–7036.

[40] W.G. Huang, X.Z. Wang, W.T. Zhang, S.J. Zhang, Y.X. Tian, Z.H. Chen, W.H. Fang, J. Ma, Intraligand charge transfer boosts visible-light-driven generation of singlet oxygen by metal-organic frameworks, Appl. Catal. B Environ. 273 (15) (2020) 119087.

[41] Y. Xu, R.Y. Zhang, J.J. Zhu, Z.Y. Guo, D. Jin, L. Qian, Y. Yang, H.G. Chen, Strategically staged tumor ablation and inflammation suppression using shell-core nanoparticles to eradicate bladder tumors and prevent recurrence, Adv. Funct. Mater. 34 (37) (2024) 2402078.

[42] Y. Park, E. Cheong, J.G. Kwak, R. Carpenter, J.H. Shim, J. Lee, Trabecular bone organoid model for studying the regulation of localized bone remodeling, Sci. Adv. 7 (4) (2021) eabd6495.

[43] B. Yuan, L.N. Wang, R. Zhao, X. Yang, X. Yang, X.D. Zhu, L.M. Liu, K. Zhang, Y. M. Song, X.D. Zhang, A biomimetically hierarchical polyetherketoneketone scaffold for osteoporotic bone repair, Sci. Adv. 6 (50) (2020) eabc4704.

[44] D.Y. Kong, Z.X. Kang, C.R. Jiang, Z.H. Zhang, X.B. Wang, Q. Han, Y.B. Shi, Reinforcement of bionic trabecular bone scaffolds for bone defect repair using the slime mould algorithm, Mater. Des. 233 (2023) 112184.

[45] Y. Cai, Z. Wei, C.H. Song, C.C. Tang, W. Han, X.C. Dong, Optical nano-agents in the second near-infrared window for biomedical applications, Chem. Soc. Rev. 48 (1) (2019) 22–37.

[46] G.L. Wu, X.F. Tan, Q.L. Yang, Recent advances on NIR-II light-enhanced chemodynamic therapy, Adv Healthc Mater 13 (10) (2024) e2303451.

[47] H.H. Xie, S.Y. Geng, J.D. Shao, G.H. Luo, Q. Liu, J.H. Wang, Y. Chen, P.K. Chu, Z. B. Li, X.F. Yu, Niobium diselenide nanosheets: an emerging biodegradable nanoplatform for efficient cancer phototheranostics in the NIR-II window, Adv Healthc Mater 11 (23) (2022) 2202126.

[48] Q.H. Zhang, Q.B. Guo, Q. Chen, X.X. Zhao, S.J. Pennycook, H.R. Chen, Highly efficient 2D NIR-II photothermal agent with Fenton catalytic activity for cancer synergistic photothermal-chemodynamic therapy, Adv Sci. 7 (7) (2020) 1902576.

[49] Z.S. Liu, C.Y. Hong, C.S. Pan, Y.Z. Sun, Y.G. Lv, Y.Y. Wei, X.F.Z. Wang, W. Zang, Q. L. Mao, X.X. Deng, P.Y. Wang, W.H. Zhu, T.X. Chen, M.X. Wu, J. Li, A.G. Wu, Synergistically enhanced chemodynamic therapy induced by NIR-II photothermal therapy with MRI/CT imaging guidance for colorectal cancer, ACS Mater. Lett. 6 (5) (2024) 1593–1605.

[50] Y.X. Xiong, C. Xiao, Z.F. Li, X.L. Yang, Engineering nanomedicine for glutathione depletion-augmented cancer therapy, Chem. Soc. Rev. 50 (10) (2021) 6013–6041.

[51] L.D. Santos, V.R. Silva, M.V.L. de Castro, R.B. Dias, L.D. Valverde, C.A.G. Rocha, M. B.P. Soares, C.A. Quadros, E.R. dos Santos, R.M.M. Oliveira, R.M. Carlos, P.C. L. Nogueira, D.P. Bezerra, New ruthenium-xanthoxylin complex eliminates colorectal cancer stem cells by targeting the heat shock protein 90 chaperone, Cell Death Dis. 14 (12) (2023) 832.

[52] M. Dodson, R. Castro-Portuguez, D.D. Zhang, NRF2 plays a critical role in mitigating lipid peroxidation and ferroptosis, Redox Biol. 23 (2019) 101107.

[53] H. Dong, Y.X. Cao, K. Zou, Q. Shao, R.H. Liu, Y. Zhang, L.Z. Pan, B. Ning, Ellagic acid promotes osteoblasts differentiation via activating SMAD2/3 pathway and alleviates bone mass loss in OVX mice, Chem. Biol. Interact. 388 (25) (2024) 110852.

[54] Z.X. Wu, L.F. Hu, K. Ru, W.J. Zhang, X. Xu, S.Y. Liu, H. Liu, Y.X. Jia, S.J. Liang, Z. H. Chen, A.R. Qian, Ellagic acid inhibits CDK12 to increase osteoblast differentiation and alleviate osteoporosis in hindlimb-unloaded and ovariectomized mice, Phytomedicine 114 (114) (2023) 154745.